The Astrophysical Journal, 975:84 (31pp), 2024 November 1 https://doi.org/10.3847/1538-4357/ad6c47

A Rapid Sequence of Solar Energetic Particle Events Associated with a Series of Extreme-ultraviolet Jets: Solar Orbiter, STEREO-A, and Near-Earth Spacecraft Observations

D. Lario[1], L. A. Balmaceda[1,2], R. Gómez-Herrero[3], G. M. Mason[4], V. Krupar[1,5], C. Mac Cormack[1,6], A. Kouloumvakos[4], I. Cernuda[3], H. Collier[7], I. G. Richardson[1,8], P. Kumar[1,9], S. Krucker[7], F. Carcaboso[10], N. Wijsen[11], R. D. Strauss[12], N. Dresing[13], A. Warmuth[14], J. Rodríguez-Pacheco[3], L. Rodríguez-García[3,15], I. C. Jebaraj[13], G. C. Ho[16], R. Bučík[16], D. Pacheco[17], F. Espinosa Lara[3], A. Hutchinson[1,5], T. S. Horbury[18], L. Rodríguez[19], N. P. Janitzek[20], A. N. Zhukov[19,21], A. Aran[22], and N. V. Nitta[23]
[1] Heliophysics Science Division, NASA Goddard Space Flight Center, Greenbelt, MD, USA; david.larioloyo@nasa.gov
[2] Physics and Astronomy Department, George Mason University, Fairfax, VA, USA
[3] Universidad de Alcalá, Space Research Group, Alcalá de Henares, Spain
[4] The Johns Hopkins University, Applied Physics Laboratory, Laurel, MD, USA
[5] Goddard Planetary Heliophysics Institute, University of Maryland, Baltimore County, MD, USA
[6] Physics Department, The Catholic University of America, USA
[7] University of Applied Sciences and Arts Northwestern Switzerland, Windisch, Switzerland
[8] Department of Astronomy, University of Maryland, College Park, MD 20742, USA
[9] Department of Physics, American University, Washington, DC 20016, USA
[10] NASA Postdoctoral Program Fellow, NASA Goddard Space Flight Center, Greenbelt, MD, USA
[11] Centre for mathematical Plasma Astrophysics, KU Leuven, 3001 Leuven, Belgium
[12] Center for Space Research, North-West University, Potchefstroom, South Africa
[13] Department of Physics and Astronomy, University of Turku, Finland
[14] Leibniz-Institut für Astrophysik Potsdam (AIP), 14482 Potsdam, Germany
[15] European Space Agency (ESA), European Space Astronomy Centre (ESAC), 28692 Villanueva de la Cañada, Madrid, Spain
[16] Southwest Research Institute, San Antonio, TX, USA
[17] Deep Space Exploration Laboratory/School of Earth and Space Sciences, University of Science and Technology of China, Hefei 230026, People's Republic of China
[18] The Blackett Laboratory, Department of Physics, Imperial College London, UK
[19] Solar-Terrestrial Centre of Excellence-SIDC, Royal Observatory of Belgium, 1180 Brussels, Belgium
[20] Institut für Teilchenphysik und Astrophysik, Eidgenössische Technische Hochschule (ETH) Zürich, 8093 Zürich, Switzerland
[21] Skobeltsyn Institute of Nuclear Physics, Moscow State University, 119991 Moscow, Russia
[22] Department of Quantum Physics and Astrophysics, Institute of Cosmos Sciences (ICCUB), Universitat de Barcelona (UB-IEEC), Spain
[23] Lockheed Martin Advanced Technology Center, Palo Alto, CA 94304, USA
Received 2024 April 17; revised 2024 June 20; accepted 2024 June 23; published 2024 October 25

Abstract

A series of solar energetic electron (SEE) events was observed from 2022 November 9 to November 15 by Solar Orbiter, STEREO-A, and near-Earth spacecraft. At least 32 SEE intensity enhancements at energies >10 keV were clearly distinguishable in Solar Orbiter particle data, with 13 of them occurring on November 11. Several of these events were accompanied by $\lesssim$10 MeV proton and $\lesssim$2 MeV nucleon^{-1} heavy-ion intensity enhancements. By combining remote-sensing and in situ data from the three viewpoints (Solar Orbiter and STEREO-A were ∼20° and ∼15° east of Earth, respectively), we determine that the origin of this rapid succession of events was a series of brightenings and jetlike eruptions detected in extreme ultraviolet (EUV) observations from the vicinity of two active regions. We find a close association between these EUV phenomena, the occurrence of hard X-ray flares, type III radio bursts, and the release of SEEs. For the most intense events, usually associated with extended EUV jets, the distance between the site of these solar eruptions and the estimated magnetic connectivity regions of each spacecraft with the Sun did not prevent the arrival of electrons at the three locations. The capability of jets to drive coronal fronts does not necessarily imply the observation of an SEE event. Two peculiar SEE events on November 9 and 14, observed only at electron energies $\lesssim$50 keV but rich in $\lesssim$1 MeV nucleon^{-1} heavy ions, originated from slow-rising confined EUV emissions, for which the process resulting in energetic particle release to interplanetary space is unclear.

Unified Astronomy Thesaurus concepts: Solar energetic particles (1491); Solar coronal waves (1995)

Materials only available in the online version of record: machine-readable table

1. Introduction

Impulsive solar energetic electron (SEE) events are small short-lived electron intensity enhancements detected in interplanetary space at energies between a few keV to hundreds of keV. These SEE events are closely associated with type III radio bursts (e.g., Lin 1985; Wang et al. 2012; Klein 2021), and often are accompanied by enriched ^{3}He and heavy-ion intensities (e.g., Lin 1985; Reames et al. 1985; Mason 2007; Wang et al. 2012). The term "impulsive," originally assigned to solar energetic particle (SEP) events associated with short-duration (<1 hr) soft X-ray (SXR) flares (Cane et al. 1986), has

been also commonly used to label these electron-rich and ^{3}He-rich SEP events that are usually associated with these short-duration flares (e.g., Reames 1990).

The solar origin of these impulsive SEP events has been related to magnetic reconnection processes on open field lines in association with solar jets (e.g., Nitta et al. 2006, 2008; Y. M. Wang et al. 2006; Krucker et al. 2011; Bučík 2020; Reames 2021, and references therein), although on some occasions these jets cannot be easily distinguished, and only just a brightening in extreme ultraviolet (EUV) coronal images can be observed (e.g., Mason et al. 2023a; Nitta et al. 2023). In other cases, large-scale activity originating from coronal jets such as EUV waves (Bučík et al. 2015, 2016) or even small narrow white-light (WL) coronal mass ejections (CMEs) has also been observed at the origin of impulsive SEP events (e.g., Kahler et al. 2001; Reames 2021). Furthermore, Lin (1985) reported that ∼45% of impulsive SEE events observed at energies above ∼15 keV are accompanied by detectable hard X-ray (HXR) bursts. These HXR bursts are generally thought to be produced by accelerated electrons traveling downward toward the high-density chromosphere (e.g., Brown 1971). Coronal nonthermal X-ray emissions at higher altitudes have also been observed in association with coronal jets although with a lower intensity than the low-altitude HXR bursts (e.g., Bain & Fletcher 2009; Glesener et al. 2012; Glesener & Fleishman 2018). The high-altitude HXR component has been interpreted as electrons escaping the Sun along open field lines producing, via bremsstrahlung mechanisms, HXR emission cospatial and cotemporal with the emerging jets (Glesener & Fleishman 2018). Statistical studies of the association between HXR flares and type III radio bursts (e.g., Reid & Vilmer 2017) and between HXR flares and coronal jets (e.g., Musset et al. 2020) indicate a close temporal association, although the correlations between HXR intensities and either type III radio flux or jet velocity and jet duration are weak. Even if all these phenomena result from the same eruptive event, the processes involved in the generation of HXR and radio emissions as well as the mechanism driving the jets are different, and hence, there are weak correlations found among these phenomena as well as large variability from event to event (e.g., Musset et al. 2020, and references therein).

The source regions of coronal jets have been found to be located in the peripheries of active regions (ARs) and coronal holes (CHs; e.g., Raouafi et al. 2016; Shen 2021; Odermatt et al. 2022, and references therein). The solar origin of ^{3}He-rich SEP events has also been identified to be in sites close to open magnetic field regions (e.g., Nitta et al. 2006; Y. M. Wang et al. 2006). All these observations are consistent with different interchange-reconnection topologies proposed in the literature for the origin of impulsive SEP events (e.g., Shibata et al. 1992; Glesener et al. 2012; Wyper et al. 2018, 2019; Battaglia et al. 2023; M. Wang et al. 2023; W. Wang et al. 2023), in which closed and open magnetic field lines reconnect where accelerated electrons and coronal jets escape along open field regions (e.g., Reames 2021, and references therein).

Factors playing a role in the observation of SEE events by a spacecraft at a given location in the heliosphere include (i) the site and properties of the particle sources, (ii) the magnetic connection established (if any) between these sources and the spacecraft, (iii) the particle transport conditions from their source to the spacecraft, as well as (iv) the field of view, energy range, and sensitivity of the particle detectors on board the spacecraft. In general, the frequency of observation of SEE events is largely dependent on the phase of the solar cycle. For example, Wang et al. (2012) reported that the occurrence rate of SEE events observed near Earth during 1995–2005 by the 3DP instrument (Lin et al. 1995) on board the Wind spacecraft (Acuña et al. 1995; Harten & Clark 1995) over three consecutive energy channels within the energy range 0.1–300 keV was $\sim$190 yr^{-1} at solar maximum but only $\sim$12 yr^{-1} at solar minimum. These rates correspond to ∼1 event every 2 days at solar maximum but only one event per month during solar minimum. At an energy of ∼40 keV, Wang et al. (2012) estimated that the rate of SEE events produced over the whole Sun was of $\sim10^4$ yr^{-1} near solar maximum but only $\sim$35 yr^{-1} at solar minimum. These rates correspond to ∼27 events per day produced over the whole Sun near solar maximum but less than three events per month during solar minimum. The frequently quoted occurrence rate of ∼1000 ^{3}He-rich events yr^{-1} in the visible solar disk during solar maximum was estimated by Reames et al. (1994) who used observations of ^{3}He-rich events from 1978 to 1991 at energies 1.3–1.6 MeV nucleon^{-1} by the Very Low-Energy Telescopes (von Rosenvinge et al. 1978) on board the third International Sun-Earth Explorer (ISEE-3; as per their definition, a ^{3}He-rich event was selected when the ion abundances integrated over the duration of the event showed a ^{3}He/^{4}He ratio greater than 0.10). The production of an event over the whole Sun or even on the visible side of the Sun does not imply the detection of the event by a spacecraft at a given heliospheric location since the accelerated particles have to reach the spacecraft, and therefore, the magnetic connection between particle sources and spacecraft as well as the particle transport processes play a predominant role (e.g., Wiedenbeck et al. 2013; Agueda & Lario 2016).

Occasionally, SEE events and ^{3}He-rich events may appear in intense sequences in association with multiple ejections from a single AR or a combination of ARs (e.g., Reames et al. 1985, 1988; Wibberenz & Cane 2006; Bučík et al. 2014, 2018, 2023; Gómez-Herrero et al. 2021; Ho et al. 2022; Mason et al. 2023a; Nitta et al. 2023; Rodríguez-García et al. 2023). In this paper, we analyze a sequence of impulsive SEE events observed during the rising phase of solar cycle 25 that occurred between 2022 November 9 and 2022 November 15. These SEE events were observed by the energetic particle suite of instruments on board Solar Orbiter (SolO; Müller et al. 2020), on the spacecraft A of the Solar TErrestrial RElations Observatory (STEREO-A, hereafter STA; Kaiser et al. 2008), and on near-Earth spacecraft such as the Solar and Heliospheric Observatory (SOHO; Domingo et al. 1995), the Advanced Composition Explorer (ACE; Stone et al. 1998), and the Wind spacecraft (Wilson et al. 2021). These SEE events occurred when two nearby ARs transited over the Earth's visible side of the Sun and generated multiple flares and coronal jets as they moved from central meridian to western longitudes. The period analyzed in this paper constitutes one of the extended ^{3}He-rich time periods observed by SolO as identified by Kouloumvakos et al. (2023). In this paper, we characterize the ion abundances observed during this period and examine the different solar phenomena associated with the origin of the SEE events. In particular, we determine the coronal EUV brightenings, EUV jets, X-ray flares, and type III radio bursts that could be associated with the origin of the SEE events and their interdependences. The structure of the paper is as follows:

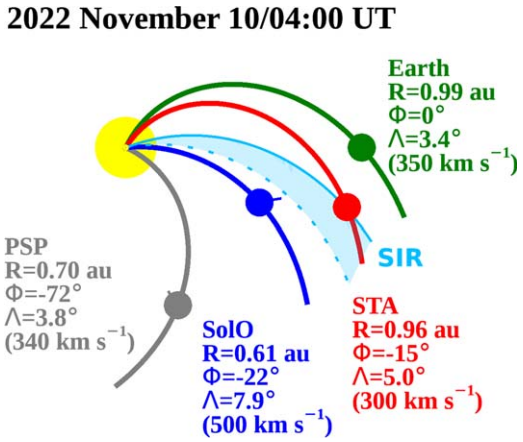

Figure 1. Schematic representation of the nominal interplanetary magnetic field configuration in the solar equatorial plane as seen from the north, showing field lines connecting the Sun to the locations of Earth (green circle), Solar Orbiter (SolO; blue circle), STEREO-A (STA; red circle), and Parker Solar Probe (PSP; gray circle) on 2022 November 10 at 04:00 UT. Nominal Parker spiral magnetic field lines have been plotted using the solar wind speed indicated next to the HEEQ coordinates of each spacecraft; R being the heliocentric radial distance, Φ the HEEQ longitude and Λ the latitude. The light blue region indicates an SIR successively observed from east to west.

Section 2 describes the properties of the SEE events at these locations (i.e., SolO, STA, and near Earth), paying attention to the electron anisotropies and intensity-time profiles at each spacecraft. We compare electron observations with proton and ion measurements and relate these observations to the interplanetary context where the events occurred. In Section 3, a whole set of remote-sensing observations are used to help determine the solar origin of the events. Section 4 analyzes the possible interdependence between these solar phenomena and the observation of the SEE events at each spacecraft. In particular, we analyze the role played by the distance between the site where these solar phenomena occurred and the region on the Sun where each spacecraft is estimated to have established magnetic connection, paying attention to the possible existence of extended particle sources driven by the EUV jets. Finally, in Section 5, we discuss the main conclusions of our analyses, and Section 6 summarizes the most significant results.

2. Overview of the Energetic Particle Events

In this section, we analyze the energetic particle measurements performed by SolO, STA, and near-Earth spacecraft from 2022 November 9 to November 15. During the period under analysis, STA was at heliocentric distance $R = 0.96$ au and at $\sim$15° east of Earth, whereas SolO was moving from $R = 0.59$ au and 23° east of Earth on 2022 November 9 to $R = 0.66$ au and 19° east of Earth on 2022 November 15. Figure 1 shows the spatial distribution of these spacecraft on 2022 November 10 at 04:00 UT in the solar equatorial plane as seen from the north. The filled circles (not to scale) indicate the locations of the Sun (yellow), STA (red), SolO (blue), and Earth (green). We also indicate in gray the location of Parker Solar Probe (PSP; Fox et al. 2016), although, during this period, PSP was performing high-speed data transfers to Earth requiring the instruments to be powered off and thus not collecting data. The legend next to each symbol in Figure 1 provides the heliocentric radial distance R, and the Heliocentric Earth Equatorial (HEEQ) longitude Φ and latitude Λ of each location. Nominal magnetic field lines connecting each one of these locations with the Sun have been plotted assuming a Parker spiral magnetic field configuration and the solar wind speed indicated in the legend next to each symbol. The light blue region indicates the presence of a solar wind stream interaction region (SIR) that was sequentially observed from east to west as discussed in Appendix A.

Figure 2 shows energetic electron intensities observed by SolO (blue traces), STA (red traces) and by spacecraft located at the Sun–Earth Lagrangian point L1 (green traces). In particular, from SolO we show in panels (a) and (b) the average of the intensities measured in the four apertures of the Electron Proton Telescope (EPT) of the Energetic Particle Detector (EPD) suite of instruments (i.e., SolO/EPD/EPT; Rodríguez-Pacheco et al. 2020), whereas in panel (c) we show 2.4–6.0 MeV electron intensities averaged over the four apertures of the EPD High Energy Telescope (HET; i.e., SolO/EPD/HET; Rodríguez-Pacheco et al. 2020). From STA, we show in panels (a) and (b) the average of the intensities measured in the four apertures of the Solar Electron and Proton Telescope (SEPT; Müller-Mellin et al. 2008), and in panel (c) the 2.8–4.0 MeV electron intensities measured by the HET (von Rosenvinge et al. 2008) of the In situ Measurements of Particles And CME Transients (IMPACT) suite of instruments (Luhmann et al. 2008) on board STA (i.e., STA/HET). From L1, we show in panels (a) and (b) spin-averaged data from the 3DP instrument on the Wind spacecraft (Lin et al. 1995), whereas in panel (c) we show 2.64–10.4 MeV electron intensities from the Electron Proton Helium INstrument (EPHIN) of the Comprehensive Suprathermal and Energetic Particle Analyser (COSTEP; Müller-Mellin et al. 1995) on board SOHO.

Figures 2(a) and (b) display the exceptional sequence of electron intensity enhancements observed at the three different locations, especially from late November 10 to late November 14. The identification of each one of these electron intensity enhancements as a separated SEE event is based on whether the intensity increased by a factor of 3σ above the prior measured intensity, kept increasing for at least three consecutive 1 minute averaged data points, and eventually reached a maximum, and either started to decay or a new event resulting from a new injection was detected (with the same 3σ condition). Prior to November 13, the SEE events at SolO were characterized by rapid onsets to a prominent peak followed by a gradual decay. By contrast, the events at STA prior to mid-November 11 displayed more gradual intensity increases with smooth rounded peaks, whereas at L1 the events with accentuated peaks were not observed until mid-November 13. Figures 2(a)–(b) also show that, for the SEE events prior to November 13, the $\lesssim$100 keV intensities observed by SolO were usually larger than at STA, whereas starting on November 13 STA intensities were larger. In Appendix B, we detail the electron anisotropies measured by the particle instruments on SolO, STA, and Wind during these events. The onset and peak of most of the electron events observed by SolO over the energies shown in Figures 2(a)–(b) were highly anisotropic whereas during the decay of the event the electron pitch-angle distributions (PADs) evolved quickly to isotropic. The peculiar configuration of the STA spacecraft during this period prevents a complete analysis of the PADs at this spacecraft (see details in Appendix B). By contrast, the events detected by Wind/3DP prior to November 14 displayed much weaker anisotropies and lower intensities

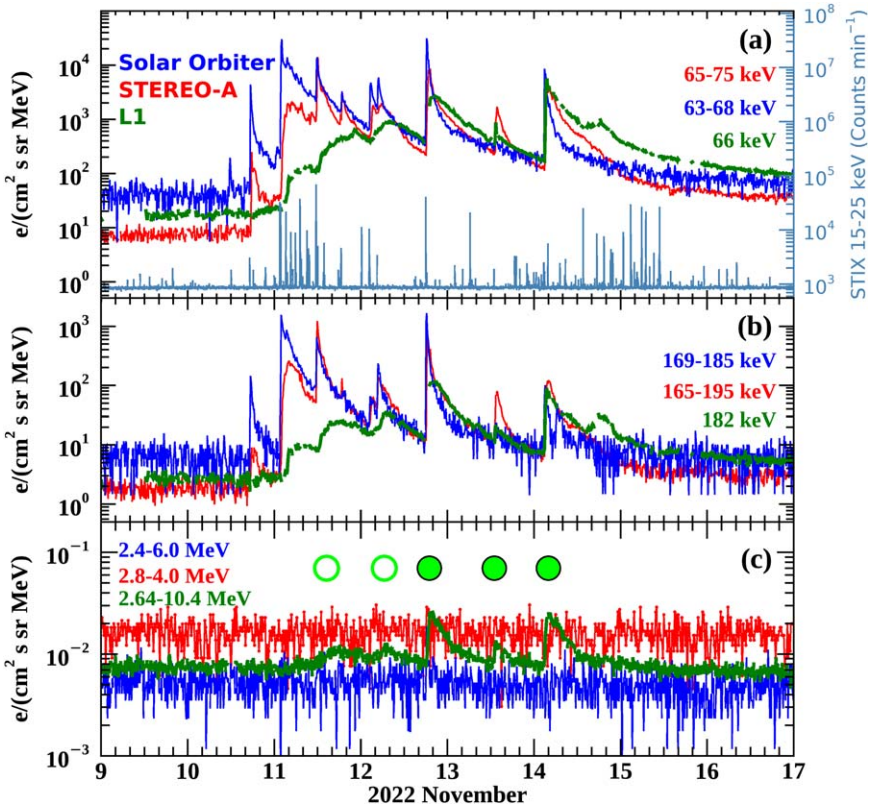

Figure 2. (a)–(b) 10 minute averages of near-relativistic electron intensities observed by EPD/EPT on board SolO (blue), by SEPT on board STA (red), and by Wind/3DP (green) at two different energies. (c) 10 minute averages of the relativistic electron intensities measured by EPD/HET on board SolO (blue), and COSTEP/EPHIN on board SOHO (green), together with 15 minute averages of the 2.8–4.0 MeV electron intensities measured by the HET telescope on board STA (red). The three solid green circles in panel (c) indicate three relativistic electron enhancements observed by SOHO at energies above ∼2 MeV with solar origin associated with CMEs. There are two additional relativistic electron enhancements at SOHO in mid-November 11 and early November 12 for which no CMEs were observed in association with their solar origin (indicated by open green circles). An additional small relativistic electron event at SOHO can be perceived early on November 11 (see Section 5 for details). Panel (a) includes 10 minute averages of the 15–25 keV X-ray intensities observed by STIX on board SolO (thin teal trace); see Section 3.1.

than in the other spacecraft, while the two events on early and late November 14 at L1 displayed anisotropic onsets.

Figure 2(c) shows electron intensities at energies above ∼2.4 MeV. Five electron intensity increases were clearly observed by COSTEP/EPHIN (green traces). We indicate with green circles these five intensity enhancements. As discussed in Section 4.2, the events labeled with solid green circles were associated with CMEs, whereas for the events with open green circles no CMEs were observed. STA/HET only detected two SEE events at these relativistic energies on November 12 (second open green circle and first solid green circle), whereas SolO/EPD/HET only detected a $\gtrsim$2.4 MeV electron intensity enhancement late on November 12 (first solid green circle). The large geometric factor of COSTEP/EPHIN, together with an active anticoincidence system in this instrument (see details in Müller-Mellin et al. 1995), allows a better detection of these relativistic electron events than that of STA/HET and SolO/EPD/HET.

The exact number of electron events observed during the period displayed in Figure 2 evidently depends on the energy considered, and on the instrument field of view and instrument sensitivity. Fortunately, the EPD suite of instruments on SolO includes the Supra-Thermal Electron Proton sensor (STEP) that measures with high sensitivity electrons with energies above ∼4 keV and overlaps with the energy coverage of EPT (Wimmer-Schweingruber et al. 2021). The STEP field of view, close to the nominal Parker spiral magnetic field direction, is similar to the sunward aperture of EPT (see Figure 4 in Rodríguez-Pacheco et al. 2020). The top panel of Figure 3 shows a spectrogram of the SolO electron intensities collected by the sunward aperture of EPT at energies $\gtrsim$35 keV and by STEP at energies $\lesssim$35 keV. Whereas some events can be tracked all the way from the highest energies detected by EPT to the lowest energies of STEP (∼4 keV), some other events are only observed at very low energies. During November 11 (November 12), up to 13 (nine) distinct >10 keV electron events can be distinguished. The number of SEE events at energies >65 keV drops to 11 (four) on November 11 (November 12), and at energies >1 MeV drops to three (one) on November 11 (November 12). The maximum energy at which these events can be observed is different from event to event. Two particularly intense events clearly distinguishable in the SolO/EPD/STEP measurements at energies below ∼45 keV and ∼58 keV occurred early on November 9 and late on November 14, respectively. These two events would have been practically unnoticed if using only SolO/EPD/EPT observations. By contrast, the number of SEE events measured by STA/SEPT (at energies >65 keV) is limited to 12 events throughout the interval under study (see Figure 2(a)). Therefore, depending on the instrument sensitivity, the particle energy, and the instrument orientation in the case of anisotropic particle flows, the number of the observed electron events varies.

For each one of these >10 keV electron intensity increases measured by SolO, we have estimated the release time of the first observed electrons. A velocity dispersion analysis (e.g.,

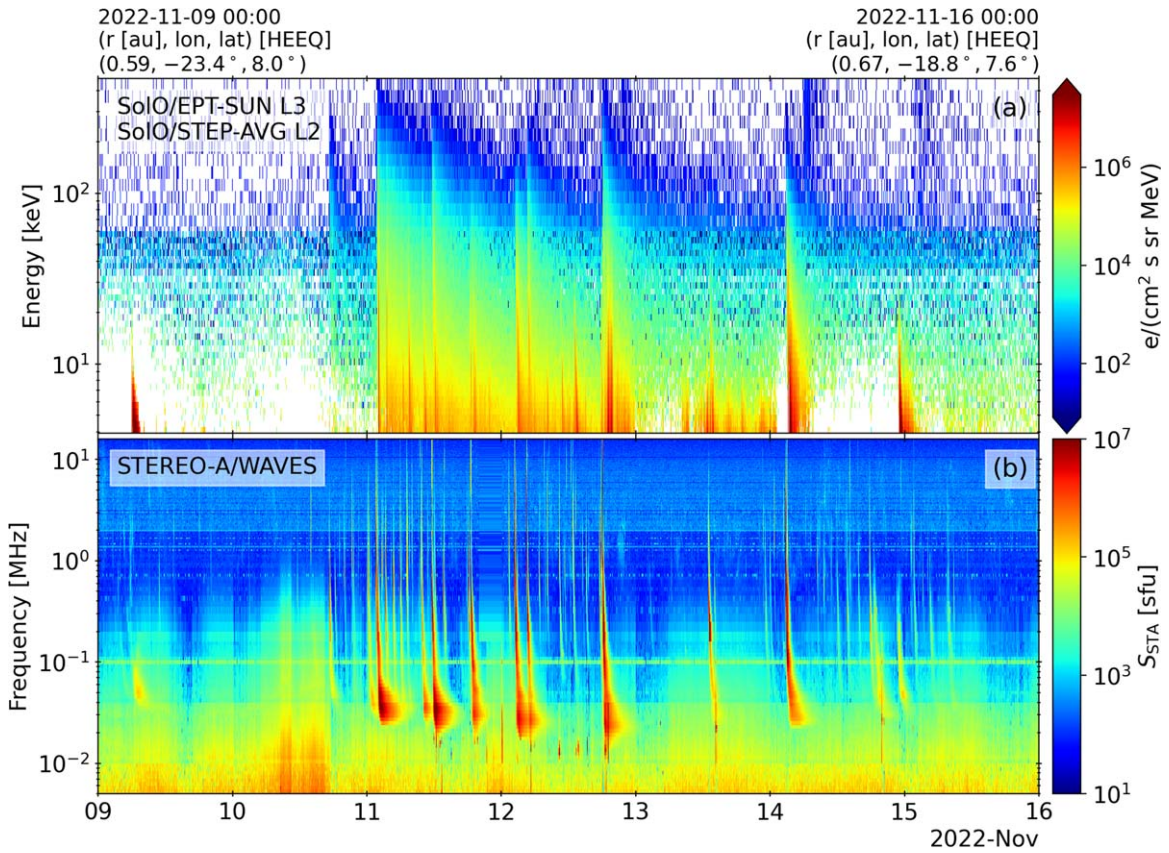

Figure 3. (a) Electron spectrograms combining intensities collected by the sunward aperture of EPT (at energies $\gtrsim$35 keV) and by STEP (at energies $\lesssim$35 keV) on board Solar Orbiter. A total of 32 $>$ 10 keV electron events with discernible onsets can be distinguished (see text for details). (b) Radio dynamic spectrum obtained from the SWAVES instrument on board STA showing the sequence of type III radio bursts (see Section 3.2).

Vainio et al. 2013) was not possible for all these events because a fit to the onset times at different energies versus the inverse of the electron speed ($1/v$) did not provide a reliable linear dependence and/or a realistic path length. These cases may result from either onset times at different energies observed under different magnetic field directions (i.e., the first electrons are observed at different pitch angles, implying that electrons of different energies followed different travel paths), incomplete pitch-angle coverage at the onset of the event, and/or that the injection of electrons at different energies did not occur simultaneously. Therefore, a time-shift analysis (TSA) method was applied to all the events to infer the electron release times. The TSA method considers that the first detected electrons traveled scatter free with a pitch angle of 0° along a nominal Parker spiral magnetic field line. The scatter-free propagation with small pitch angle seems a reasonable assumption given the large anisotropies measured at the onset of most of the SEE events (see Appendix B). The arrival times of the first electrons have been obtained by using 1 minute averages of the particle intensities and requiring an intensity increase above a factor of 3σ of the pre-event intensity as measured by the aperture of EPD/EPT that first detects an electron intensity increase. In the case of low-energy SEE events observed only by EPD/STEP, the intensity averaged over all the pixels of EPD/STEP has been used (Rodríguez-Pacheco et al. 2020). The length of the Parker spiral magnetic field line has been computed considering the measured solar wind speed or a nominal 400 km s^{-1} when solar wind measurements are not available. The assumptions made in the TSA method could also differ from the actual transport conditions undergone by the SEEs, and therefore, the estimates of the particle release times should be considered as approximate values when compared with the timing of the solar phenomena analyzed in this paper (Section 3). Details about the methods used to infer particle release times and their limitations can be found, for example, in Gómez-Herrero et al. (2021) or Vainio et al. (2013).

Table 1[24] lists the solar phenomena typically associated with the origin of the SEE events observed during the period under analysis (see details in Section 3), together with the estimated release time of the $>$10 keV electron events observed by SolO, as well as the maximum energy for which an electron intensity increase was observed. A total of 32 SEE events were observed by SolO/EPD at energies $>$10 keV. The times listed in column (8) of Table 1 are the estimated times when the first electrons were released at the Sun (i.e., the solar release times or SRTs). Therefore, when comparing them with the times of the solar phenomena associated with the origin of the SEE events (i.e., HXR emission, EUV jets, and type III radio bursts), it would be necessary to consider the light transit time in the remote-sensing detection of these solar emissions (see Section 4). The electron energy assumed to infer the SRTs listed is either 43 keV (the average energy of the first six energy channels of EPT) or the maximum energy of the event if it was only observed below 43 keV. SRTs are given with a resolution of

[24] The complete table is available in its entirety in machine-readable form.

Table 1
List of Solar Phenomena and SEE Events in Chronological Order

Date (yyyy-mm-dd)	STIX 15–25 keV Flare			NOAA/SWPC Flare Report GOES X-Ray Onset/Max[b] Class for NOAA AR Flare Location	EUV Jets/Brightenings/CFs		Type III	SolO e^- SRT (Energy Range)
	Peak Time (hh:mm:ss)[a]	Peak Intensity (cts 4 s bin^{-1})	STIX Location		Flag[c]/Onset Time[d]/ Type[e]	Location	1 $R_\odot$ Time[f] (hh:mm:ss)	
(0)	(1)	(2)	(3)	(4)	(5)	(6)	(7)	(8)
2022-11-11	04:35:00 (04:29:52)	991	N12W08	04:33/04:41 (04:25/04:33) C3.3 AR 13141 SF N14W03	E/04:36 (04:28)/jet	N13W07	04:32:10	04:32 ($\lesssim$200 keV)
2022-11-11	05:10:12 (05:05:04)	247	N12W08	05:07/05:14 (04:59/05:06) B7.8 AR 13141	E/05:13 (05:05)/jet	N12W08	...	...
2022-11-11	05:51:44 (05:46:36)	863	N12W08	05:46/05:56 (05:38/05:48) C1.9 AR 13141	E/05:52 (05:44)/broken CF	N13W08	05:47:26	05:50 ($\lesssim$130 keV)

Notes. Date of the observation (column (0)), HXR flares detected by SolO/STIX (columns (1)–(3)), SXR flares detected by GOES-16 (column (4)), EUV jets and brightenings observed in SDO/AIA 193 Å images (columns (5)–(6)), release time of electrons producing type III radio bursts observed by STA/SWAVES (column (7)), and estimated SRTs for the SEE events observed by SolO/EPD (column (8)). Table 1 is published in its entirety in the machine-readable format, where Time-STIX and STime-STIX are the times listed in column (1), Peak-STIX are the peak values listed in column (2), Loc-STIX are the locations listed in column (3), Time-EUV and STime-EUV are the times listed in column (5), Loc-EUV are the locations listed in column (6), STime-Type3 are the times listed in column (7), and STime-SEE are the release times listed in column (8).

[a] The times listed for the HXR flares are the peak time of the 15–25 keV HXR emission as observed by SolO/STIX, and in parentheses, the time shifted back to the Sun by considering the light transit time from Sun to the spacecraft.

[b] The times listed for the SXR flares are the onset and peak of the SXR emission as reported by NOAA/SWPC (in parentheses are the same times shifted back to the Sun).

[c] Flag E indicates when the EUV brightening is seen as an EUV emission increase in Figures 7(b) and 8(b).

[d] The times for the EUV jets and brightenings are the onset times of the emission as seen in SDO/AIA 193 Å images (in parentheses, the times shifted back to the Sun).

[e] Type of EUV emission as described in Section 3.3; brightening (B), extended jet (EJ), coronal front (CF).

[f] Type III 1 $R_\odot$ times inferred using STA/SWAVES data except for those events indicated by So when SolO/RPW data were used.

(This table is available in its entirety in machine-readable form in the online article.)

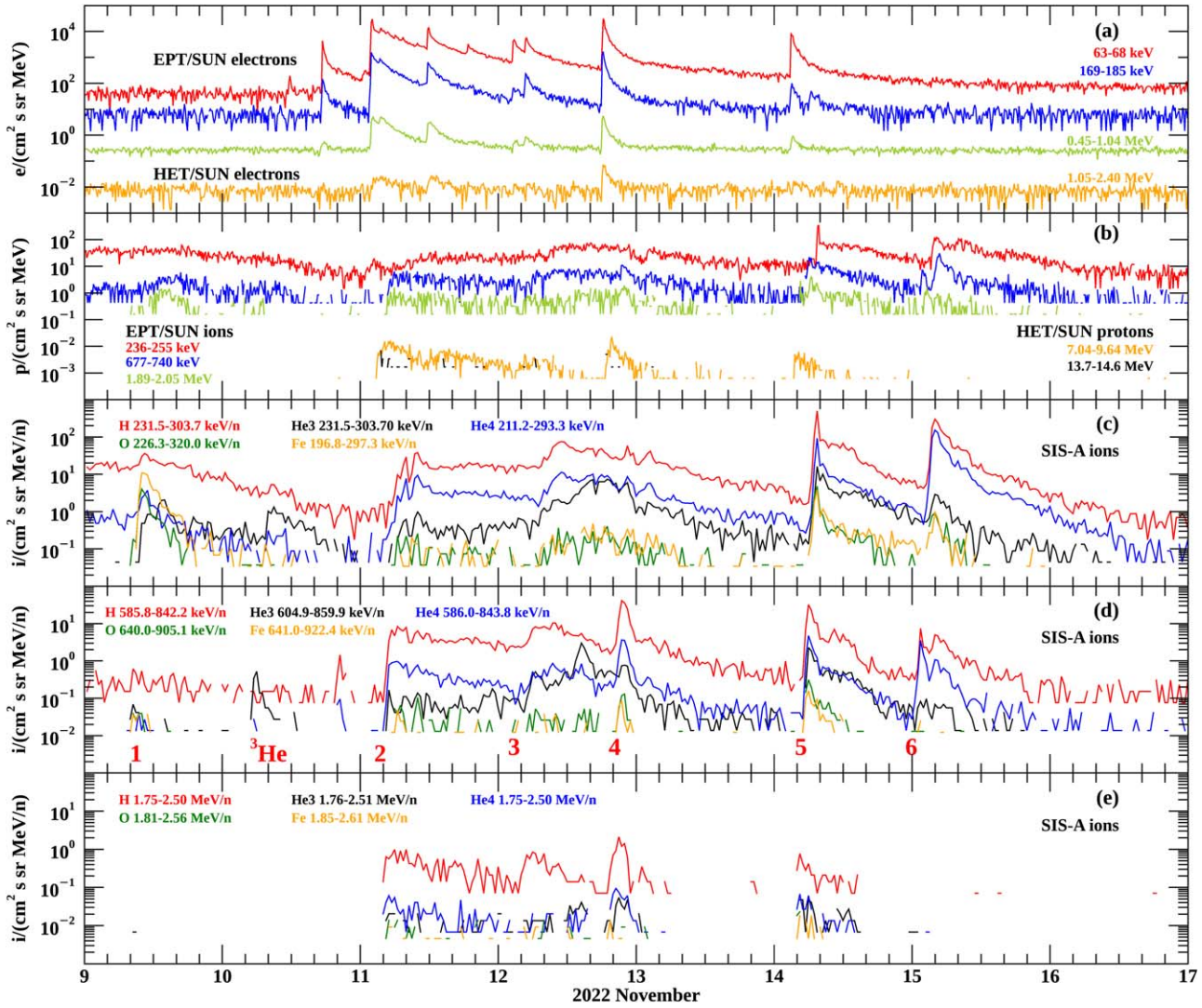

Figure 4. (a) 10 minute averages of the electron intensities measured by the sunward apertures of EPT (three top traces) and of HET (orange trace); (b) 10 minute ion intensities measured by the sunward aperture of EPT (three top traces) and proton intensities measured by the sunward aperture of HET (orange and black traces); (c)–(e) 30 minute averages of the H (red), ^{3}He (black), ^{4}He (blue), O (green), and Fe (orange) ion intensities at (c) ∼250 keV nucleon^{-1}, (d) ∼700 keV nucleon^{-1}, and (e) ∼2 MeV nucleon^{-1}. In panel (d), the numbers 1 through 6 identify the distinctive low-energy ion intensity enhancements observed during this period, whereas ^{3}He identifies an extremely ^{3}He-rich intensity enhancement observed early on November 10.

1 minute following the method described above, although the errors associated with these values can be longer due to poorly defined SEE event onsets, and the fact that the actual travel path followed by the particles may differ from the assumed nominal Parker spiral field lines.

2.1. Ion Abundances

The Suprathermal Ion Spectrograph (SIS) of the EPD suite of instruments on SolO measures ion composition from protons through ultraheavy nuclei over the energy range ∼0.1–10 MeV nucleon^{-1} (Rodríguez-Pacheco et al. 2020; Wimmer-Schweingruber et al. 2021). SIS is a time-of-flight mass spectrometer consisting of two identical telescopes, one facing sunward (telescope A) along the nominal Parker spiral magnetic field direction and the other (telescope B) pointing antisunward at an angle of 130° with respect to telescope A (Rodríguez-Pacheco et al. 2020). The three bottom panels of Figure 4 show ion intensities (H, ^{3}He, ^{4}He, O, and Fe in red, black, blue, green, and orange, respectively) at three different energies as measured by the telescope A of SIS (i.e., SIS-A). The two top panels of Figure 4 show (a) electron intensities observed by the sunward apertures of SolO/EPD/EPT and SolO/EPD/HET at different energies, and (b) ion intensities measured by the sunward aperture of SolO/EPD/EPT and proton intensities measured by the sunward aperture of SolO/EPD/HET. Note that SolO/EPD/EPT does not distinguish ion species, so the red, blue, and green traces in Figure 4(b) refer to ions in general, although the intensities are presumably dominated by protons. The orange trace and the discrete black dots in Figure 4(b) are proton intensities measured by SolO/EPD/HET. Note that at proton energies above ∼13 MeV (black traces in Figure 4(b)) only discrete counts were detected by SolO/EPD/HET throughout this time interval. In Figure 4(d), the numbers 1 through 6 identify six distinct ion intensity enhancements measured by SolO/SIS. These six ion intensity enhancements are clearly evident in the ion measurements from SIS as explained below when describing Figure 5.

Whereas the electron intensity-time profiles in Figure 4(a) show several distinct enhancements caused by single episodes

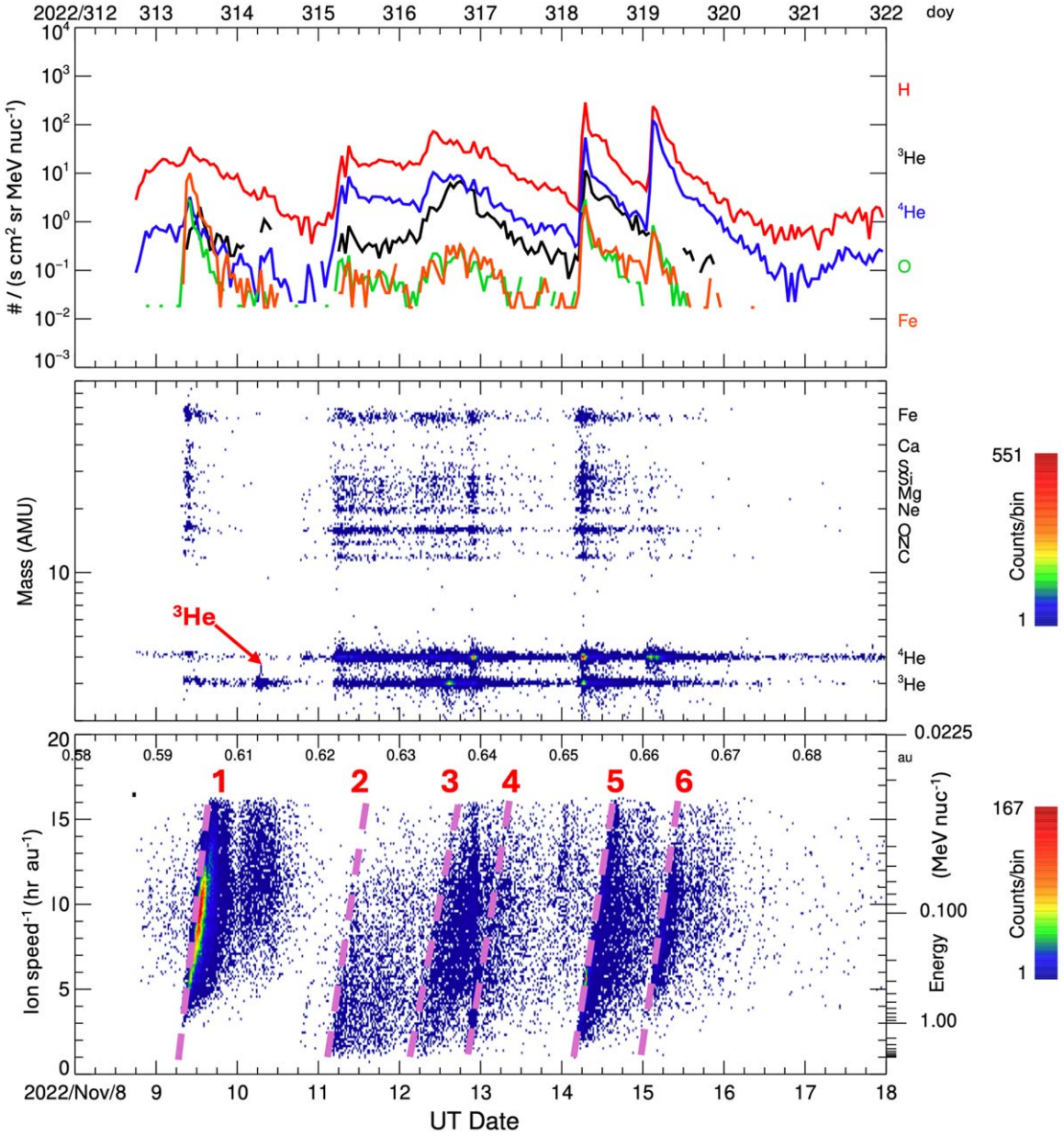

Figure 5. From top to bottom: Time profiles of 0.23–0.32 MeV nucleon^{-1} H (red), ^{3}He (black), ^{4}He (blue), O (green), and Fe (orange) ion intensities; mass spectrogram for elements from He to Fe for ions with energies 0.3–10 MeV nucleon^{-1}; and 1/ion speed vs. time of arrival for ions of mass 10–70 AMU. The dashed oblique lines indicate ion increases with velocity dispersion signatures. The dispersionless low-energy ion intensity enhancement late on November 12 is due to a local spatial magnetic field enhancement (see Figure A1(c1)) whereas at higher energies were due to the onset of the ion event #4.

of solar electron injections (see discussion in Section 4), low-energy ion intensity-time profiles measured by SIS show more irregular and long-lasting integrated intensity-time profiles with possibly unresolved ion injections. For example, throughout November 11, three clear distinct electron intensity enhancements can be distinguished at energies $\gtrsim$500 keV (or 11 events above ~65 keV, see Table 1), but only a single irregular event can be resolved in the low-energy ion intensity-time profiles (event #2 in Figure 4(d)). The events on November 9 and late on November 14 (events #1 and #6 in Figure 4) were very prominent at low-energy ($\lesssim$1 MeV nucleon^{-1}) ion intensities (Figures 4(c)–(d)), but barely any increase was seen at higher energies (Figure 4(e)) or at >63 keV electrons (Figure 4(a)). These two events were only observed at electron energies below ~45 keV and ~58 keV, respectively (see Figure 3(a)). It is also notable, in Figures 4(c) and (d), the increase in ^{3}He counts observed early on November 10 (labeled ^{3}He in Figure 4(d)) but without any clear increase in electron intensities at any energy recorded by SolO/EPD (see Figure 3(a)).

The only significant ion intensity increases at energies ~2 MeV nucleon^{-1} in Figure 4(e) correspond to the ion events #2, #3, #4, and #5. For these events, SolO/EPD/HET detected also proton increases at energies $\gtrsim$7 MeV (orange trace in Figure 4(b)), but only discrete counts at proton energies above ~13 MeV (black dots in Figure 4(b)). Figure A1 of Appendix A shows that the SEP events at STA reached similar proton energies as the SEP events at SolO, whereas only

SOHO detected a minor proton intensity increase at energies above 25 MeV in association with the ion event #5 early on November 14.

Figure 5 shows SolO/EPD/SIS observations from 2022 November 8 to 2022 November 18. The top panel shows intensities of 230–320 keV nucleon^{-1} H (red), ^{3}He (black), ^{4}He (blue), O (green), and Fe (orange) from SIS-A. Late on November 8 and early on November 9, both H and ^{4}He intensities were elevated, probably due to the effects of the SIR passage by SolO (see Appendix A). The middle panel of Figure 5 shows mass tracks for elements from He to Fe for energies 0.4–10 MeV nucleon^{-1}. The bottom panel shows a spectrogram of 1/ion speed versus time for ions with atomic mass unit (AMU) in the range 10-70 AMU. Increases with velocity dispersion signatures have been indicated with dashed oblique lines that correspond to the onset of the events labeled with the numbers 1 through 6 in Figure 4(d). The isolated event with elevated ^{3}He intensities early on November 10 but hardly any ^{4}He counts (labeled ^{3}He in Figures 4(d) and 5) stands out in the mass tracks of the middle panel in Figure 5. These kind of events with practically no measurable ^{4}He in plots such as Figure 5 are due to a rollover of the ^{4}He spectrum below 400 keV nucleon^{-1} (the threshold for the plot window) but with the ^{3}He spectrum extending to higher energies into the plot window, as previously reported by Ho et al. (2019).

By considering each blob of dots separated by the slanted dashed lines in the bottom panel of Figure 5 as a different event, we have computed, for each one of the indicated EPD/SIS events, the ^{3}He/^{4}He and Fe/O abundance ratios at the energies 0.5–2.0 MeV n^{-1} and 0.32–0.45 MeV n^{-1}, respectively (see Table 2). The event #1 on November 9 stands out for its elevated Fe/O ratio. In fact, this event was extremely rich in ultraheavy ions (we refer the reader to Mason et al. 2023b for details on the compositional signatures of this event). By considering the inclined dashed lines in the bottom panel of Figure 5, we infer an approximate release time of the ions that formed each one of the ion events observed by SolO/EPD/SIS (listed in column (4) of Table 2). In column (5) of Table 2, we transcribe the electron SRT from column (8) of Table 1 for those electron events that originated around the time of the ion releases at the onset of the corresponding ion event. The estimated ion release times seem to be delayed with respect to the electron SRTs. Such delays in the injection of ions with respect to electron injections have been previously reported (e.g., Reames et al. 1985; Ho et al. 2003; Wang et al. 2016). However, there are greater uncertainties in the ion release times inferred from SIS measurements than in the electron release times. The longer ion flight times introduce larger uncertainties in the ion release times than in the case of electrons (e.g., Janitzek et al. 2024, in preparation).

The SEE events corresponding to the ion events #2, #4, and #5 were the most intense SEE events at energies $\lesssim$60 keV observed by SolO throughout the interval under study (Figure 4(a)). The most intense ~65 keV SEE events at STA occurred in mid-November 11 during the ion event #2 and late on November 12 in association with the ion event #4, whereas at L1 the most intense SEE event occurred early on November 14 in association with the ion event #5. We note that, during this period, the Suprathermal Ion Telescope (SIT; Mason et al. 2008) on board STA detected only a diffusive low-energy ion intensity increase from late November 10 to November 16 with an initial energy-dispersionless peak early on November 11. These ion intensity profiles (not shown here) were similar to the $\lesssim$1 MeV proton intensities measured by STA/SEPT (blue and red traces in Figure A1(b2) in Appendix A) and most likely were affected by the passage of the SIR by this spacecraft. Whereas the whole period at STA displayed ion abundances consistent with ^{3}He-rich events, the individual distinct events at STA were not well resolved. Owing to the configuration of STA spacecraft during this period in which STA/SIT pointed perpendicular to the nominal Parker spiral direction (see details in Appendix B), the onsets of the presumably anisotropic events were not observed at STA making individual events less distinct. The Ultra-Low-Energy Isotope Spectrometer (ULEIS; Mason et al. 1998) on board ACE detected a diffusive gradual low-energy ion intensity enhancement on November 12 during the passage of the SIR by this spacecraft and a more impulsive event early on November 14 for which the event-integrated 0.5–2.0 MeV n^{-1} ^{3}He/^{4}He ratio is 0.22 ± 0.01, and the 0.32–0.45 MeV n^{-1} Fe/O ratio is 1.52 ± 0.07. This event corresponds to event #5 in Figure 4(d).

3. Overview of the Associated Solar Phenomena

As described in Section 1, the solar phenomena typically associated with the origin of impulsive SEP events include coronal jets, HXR flares, and type III radio bursts. In this section, we describe the observations of these phenomena from 2022 November 9 to November 14 inclusive. The association of these phenomena with the origin of the observed SEE events is described in Section 4.

3.1. X-Ray Flaring Activity

The thin teal line in Figure 2(a) shows the 15–25 keV X-ray counts collected over 1 minute intervals by the Spectrometer/Telescope for Imaging X-rays (STIX; Krucker et al. 2020) on board SolO. Although there are more X-ray enhancements than SEE events, the onset of the ~66 keV electron events shown in Figure 2(a) coincide, in general, with the occurrence of a 15–25 keV X-ray count rate enhancement; although an inspection of the figure shows that the 15–25 keV X-ray intensity increase is not well correlated with the electron intensity measured by SolO/EPD. Column (1) of Table 1 lists, for each single HXR flare, the time when the 15–25 keV X-ray count rate peak was measured. In parentheses, we indicate the time of the peak shifted back to the Sun by taking into account the heliocentric distance of SolO and the light transit time so that it can be compared with the electron SRTs listed in column (8). Column (2) lists the 15–25 keV X-ray peak intensity of each single HXR emission in units of the counts measured by STIX in bins of 4 s. STIX data allow us to locate the origin of the X-ray emission (e.g., Massa et al. 2023). Column (3) provides the location of the STIX flares given primarily by the STIX science flare list,[25] but using different count thresholds. For those small flares not included in the STIX flare list, the locations were obtained manually using the same method. Specifically, the location of the maximum X-ray intensity was found first in a full-disk back-projection map reconstructed from STIX data. Then, the source parameters (including its location) were fitted with a single singular Gaussian using a forward-fitting algorithm based on visibilities (Volpara et al. 2022). Note that every single flare listed in Table 1 may be

[25] github.com/hayesla/stix_flarelist_science

Table 2
Ion Composition Ratios for Each SolO/EPD/SIS Event

Event (1)	^{3}He/^{4}He[a] (2)	Fe/O[b] (3)	Estimated Ion SRT (4)	Estimated e$^-$ SRT (5)	Most Likely Solar Origin (6)
#1	2.19 ± 0.52	2.66 ± 0.25	09 Nov/∼06:28 UT	05:47 UT	either small brightening at N24E01 at 05:45 UT or slow confined eruption without clear jet from N33W33
^{3}He	24.3 ± 9.1	…	…	…	unknown
#2	0.219 ± 0.009	0.62 ± 0.10	11 Nov/∼02:24 UT	01:42 UT	coronal front originating at 01:25 UT from N13W05 followed by a brightening from the same region at 01:40 UT
#3	1.25 ± 0.03	0.92 ± 0.13	12 Nov/∼02:48 UT	02:17 UT	coronal front originating at 02:11 UT from N12W18
#4	0.36 ± 0.02	0.93 ± 0.24	12 Nov/∼19:00 UT	17:52 UT	coronal front originating at 17:44 UT from N12W28 and coronal front with CME at 17:53 UT from N13W27
#5	0.84 ± 0.02	1.04 ± 0.10	14 Nov/∼02:48 UT	02:37 UT	brightening at 02:36 UT at N26W32 followed by extended jet with CME at 02:39 UT from N24W34
#6	0.12 ± 0.01	1.00 ± 0.26	14 Nov/∼23:35 UT	22:31 UT	slow-rising confined eruption without clear jet from N10W34 at ∼22:32 UT

Notes.
[a] ^{3}He/^{4}He ratios computed over the energy range 0.5–2.0 MeV nucleon^{-1}.
[b] Fe/O ratio computed over the energy range 0.32–0.45 MeV nucleon^{-1}.

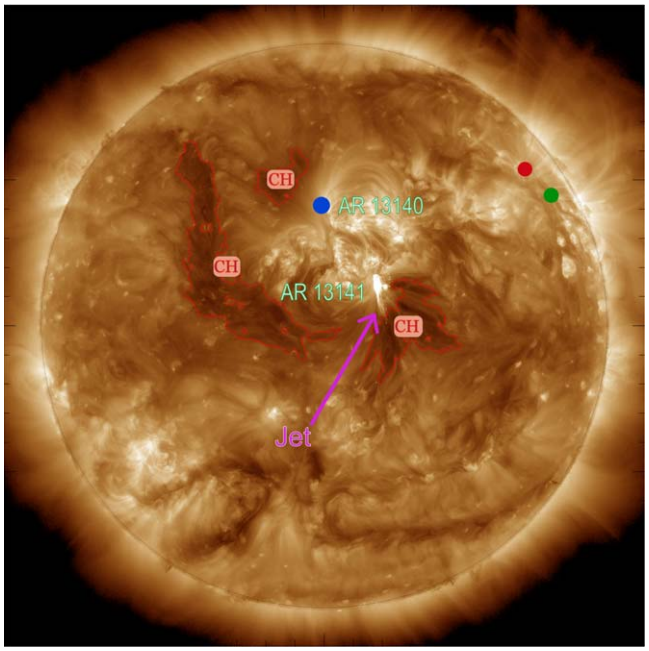

Figure 6. SDO/AIA 193 Å image taken on 2022 November 11 at 11:41 UT. At that time, NOAA ARs 13140 and 13141 were located close to central meridian. An EUV jet is observed at the southwestern edge of AR 13141. The red contours identify coronal holes (CH) surrounding the ARs. The blue, red, and green dots indicate the footpoint locations of the nominal field lines connecting to SolO, STA, and L1, respectively.

constituted of multiple HXR emissions. The grouping of a cluster of peaks as a single flare listed in Table 1 is based on both a visual inspection of the intensity-time profiles and an analysis on whether these peaks originated from the same region. Although the X-ray emission in typical solar flares may originate from two or even three emission sites (e.g., Krucker et al. 2008), the locations provided in column (3) of Table 1 correspond to the centroid of the most intense thermal source. We indicate with the label "no pixel data" in column (3) of Table 1 those STIX flares for which measurements allowing flare location were unavailable.

For completeness, in column (4) of Table 1, we have added the SXR flares provided by the Solar and Geophysical Data (SGD) event reports[26] of the National Oceanic Atmospheric Administration (NOAA) Space Weather Prediction Center (SWPC) during this time interval. These reports are based on the 0.1–0.8 nm (1.5–12 keV) X-ray flux measurements by the Geostationary Operational Environmental Satellites (GOES). The listed times in column (4) of Table 1 are the observation times of the onset and peak of the SXR flare, whereas the times listed in parentheses are when the onset and peak of the SXR flare occurred on the Sun. In general, the sites of the GOES/SXR flares are consistent with the STIX locations. Most of the X-ray activity during this period originated from two adjacent ARs (i.e., NOAA ARs 13140 and 13141).

Figure 6 shows a 193 Å image taken by the Atmospheric Imaging Assembly (AIA; Lemen et al. 2012) instrument on board the Solar Dynamics Observatory (SDO; Pesnell et al. 2012) at 11:41 UT on 2022 November 11 indicating the location of the two neighboring ARs producing most of the X-ray solar flares at the origin of the SEE events. An EUV jet in the southwest edge of AR 13141 can be observed (indicated by the purple arrow) that originated at 11:26 UT (solar time) from a location near to the concomitant GOES class M1.2 SXR flare at N12W11 (see Table 1; EUV jets will be discussed in more detail in Section 3.3). This X-ray flare and jet were most likely associated with the origin of the large SEE event observed by SolO around midday on November 11 (Figure 2), which reached $\lesssim$2 MeV energies (orange trace in Figure 4(a)), and was observed also as a 7–10 MeV proton event (orange trace in Figure 4(b)). Any possible contribution to the low-energy ion intensities was obscured by the ongoing event #2. The red contours in Figure 6 indicate CHs near the two adjacent ARs identified using the solarsoft Collection of Analysis Tools for Coronal Holes[27] (Heinemann et al. 2019). An elongated CH in the eastern hemisphere of the Sun extended from the northeast to south of AR 13141. Two other CHs were found northeast of AR 13140 and at the southwest edge of AR 13141 next to the region where the jet propagated. The presence of CHs near the regions where EUV jets originated indicates the presence of open field lines that facilitate the escape of accelerated particles (e.g., Nitta et al. 2006). The blue, red, and green dots in Figure 6 indicate the nominal site of the magnetic footpoints connecting to SolO, STA, and spacecraft located near the Sun–Earth Lagrangian L1 point such as SOHO, ACE, and the Wind spacecraft. The computation of these magnetic connecting footpoints is described below in Section 4.1. We emphasize that the large distance between the magnetic footpoints and the site of both the flare and associated jet in Figure 6 did not prevent the arrival of electrons at all three spacecraft as shown in Figure 2, in particular for STA and near-Earth spacecraft.

3.2. Type III Radio Bursts

Figure 3(b) shows the dynamic spectrum of radio emissions observed by the radio and plasma wave instrument (SWAVES; Bougeret et al. 2008) on board STA. Radio observations by the Radio and Plasma Waves (RPW) instrument (Maksimovic et al. 2020) on board SolO exhibit patterns comparable to those depicted in Figure 3(b). However, due to the superior data quality at the high frequency range of STA/SWAVES with respect to SolO/RPW (Maksimovic et al. 2021), we choose to exclusively show data from STA/SWAVES here for a cleaner and more definitive analysis. Figure 3 shows that the most intense SEE events correspond well with intense type III radio bursts that start at high ($\sim$16 MHz) frequencies and extend to almost the local plasma frequency. For those type III radio bursts when drift at different frequencies is clearly apparent, we infer the release time at the Sun of the electrons producing the type III emission as listed in column (7) of Table 1. Our methodology for inferring these release times is rooted in an empirical electron density model by Kruparova et al. (2023), which translates observed frequencies into radial distances. The assumptions are that the type III radio bursts originate as fundamental emissions, and the exciter beams move at constant speeds. These speeds are calculated from the observed frequency drift coupled with the applied density model. Consequently, we are able to trace the electron beams back to their solar surface origin, enabling us to estimate their onset times as listed in column (7) of Table 1.

[26] www.swpc.noaa.gov/products/solar-and-geophysical-event-reports

[27] github.com/sgheinemann/CATCH

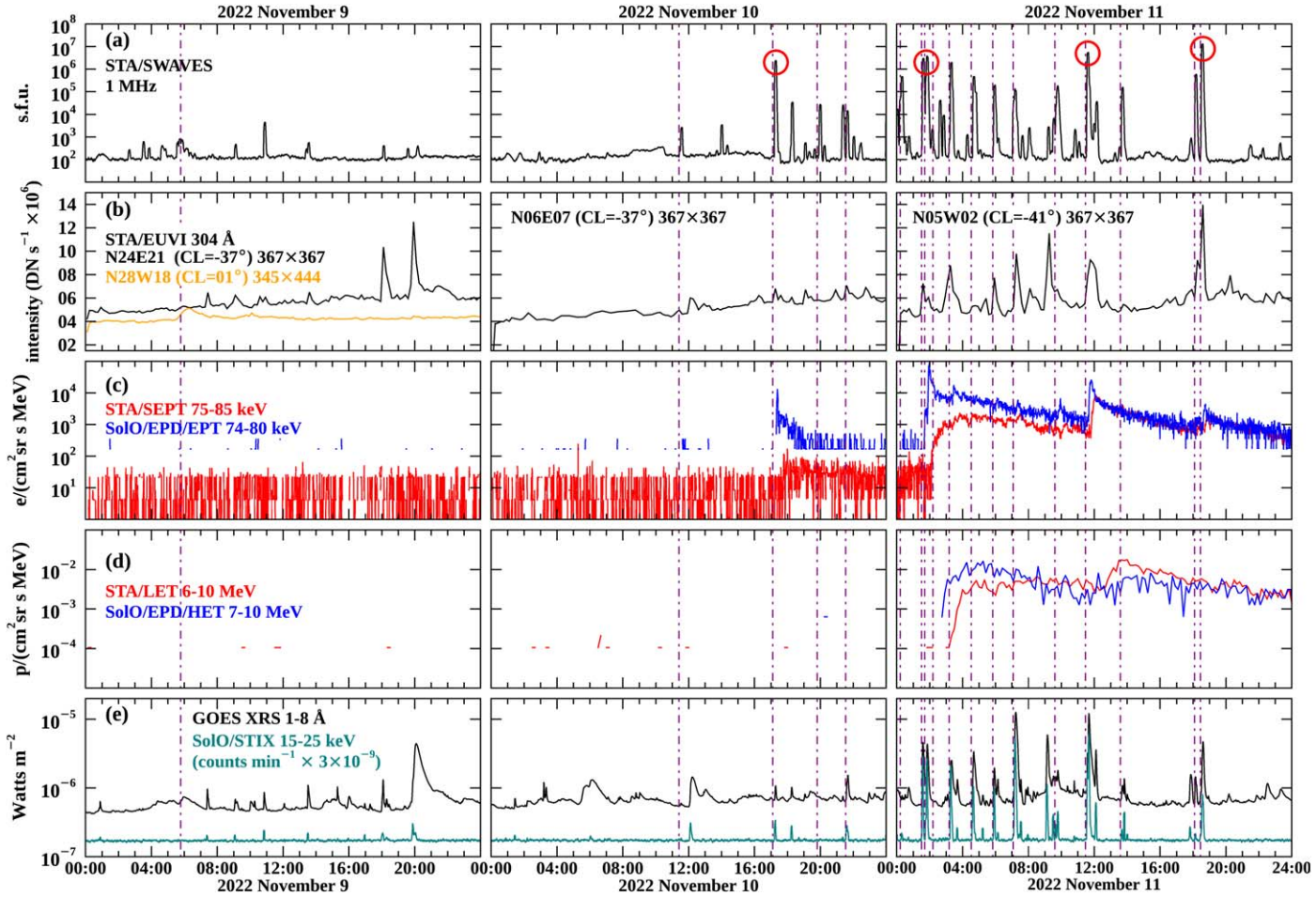

Figure 7. From top to bottom: (a) Intensity of the type III radio emissions detected by STA/SWAVES at 1 MHz; (b) 304 Å EUV intensity integrated over the indicated area where the main jets were detected using STA/EUVI observations (details are given in the text); (c) ∼75 keV electron intensities as measured by the sunward apertures of STA/SEPT (red) and SolO/EPD/EPT (blue); (d) ∼6–10 MeV proton intensities detected by STA/LET (red) and SolO/EPD/HET (blue); (e) 1–8 Å SXR intensities measured by GOES (black) and 12–25 keV HXR count rates provided by SolO/STIX (teal). The vertical dotted–dashed lines indicate the estimated electron release times as listed in column (8) of Table 1. The red circles in panels (a) indicate the type III radio bursts for which Langmuir waves were observed in situ by STA/SWAVES (see Section 3.2).

Some of the type III radio bursts extended to low frequencies and produce local Langmuir waves. The observation of these Langmuir waves indicates that the electron beams causing the type III radio emissions associated with these intense SEE events are able to reach the spacecraft location (e.g., Lin 1990; Ergun et al. 1998). Using STA/SWAVES observations, Langmuir waves were detected for periods of approximately ∼20 minutes, starting at ∼18:00 UT on November 10; ∼02:20 UT, ∼11:50 UT, and ∼18:50 UT on November 11; ∼02:45 UT, ∼04:50 UT, and ∼18:20 UT on November 12; ∼14:15 UT on November 13; and ∼03:20 UT on November 14. These time intervals correspond to the times of the most intense SEE events observed by STA (see Figures 2(a)–(b) and Figures 7 and 8 below in Section 4). Apart from these periods, RPW on SolO also observed clear Langmuir waves at ∼06:00 UT on November 9 and at ∼23:05 UT on November 14 corresponding to the onset of the ion events #1 and #6 and associated low-energy SEE events (Figure 4). The majority of observed Langmuir waves are consistent with type III radio bursts generated by fundamental emission.

An inspection of Figure 3 reveals that the intense low-energy electron events associated with the ^{3}He and Fe-rich ion events #1 and #6 in Figure 5 observed early on November 9 and late on November 14 occurred in association with type III radio bursts starting at frequencies below ∼1 MHz and with clear drifting signatures observed just below $\lesssim$76 kHz and $\lesssim$153 kHz, respectively. The radio emission signatures at higher frequencies were more complex and much weaker. The lack of high frequency emissions for these two type III radio bursts may indicate that the bursts originated on the far side of the Sun (e.g., Dulk et al. 1985). However, this is unlikely here since their association with the SEE events and related EUV emissions (see Section 4 below) clearly indicates that these events originated from the visible side of the Sun. Therefore, the lack of radio emission at higher frequencies may suggest that either (i) the energy density of the initial electron beams was not sufficient to produce a substantial amount of waves that translated into detectable radio emission (e.g., Li et al. 2008, 2009; Reid & Kontar 2018), or (ii) the environmental conditions, such as the background electron density gradient or the density fluctuations responsible for radio wave scattering, in the region where the electron beams started to propagate, were not appropriate to generate Langmuir waves (Voshchepynets et al. 2015). In order to produce radio emission starting at low frequencies, the initial electron beam has to remain stable as it

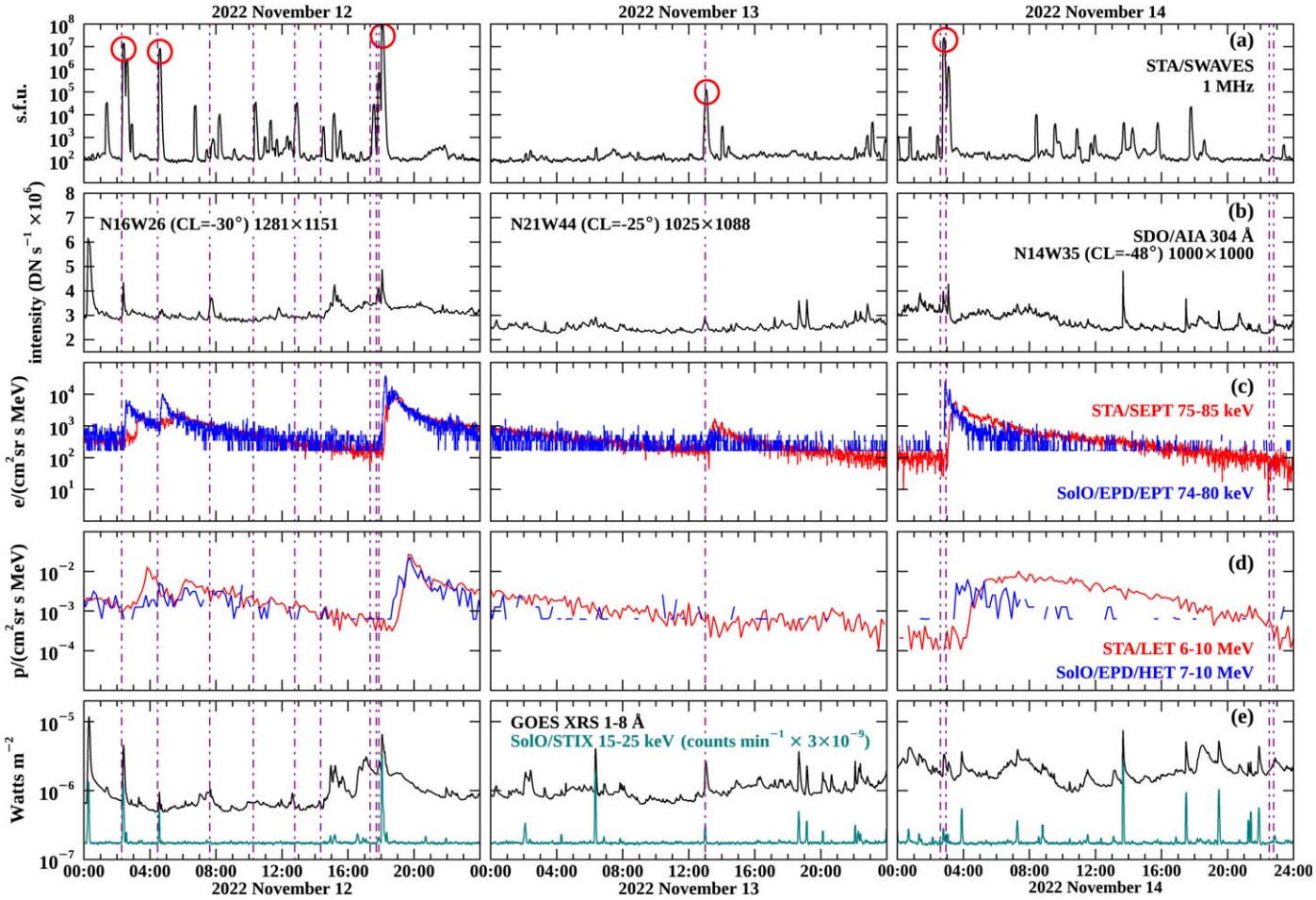

Figure 8. The same as Figure 7 but using SDO/AIA 304 Å observations in panels (b).

reaches higher altitudes with enough energy density to produce a detectable type III radio burst.

No interplanetary type II radio bursts were detected during the time interval analyzed in this study. However, as reported by Hou et al. (2023), a metric type II radio burst at high frequencies (>160 MHz) was observed at ∼02:25 UT on 2022 November 12 in association with a coronal EUV jet that appeared in SDO/AIA 193 Å images at 02:19 UT from the same edge of the AR 13141 as the jet shown in Figure 6. No CME was seen in association with this EUV jet and metric type II radio burst (Hou et al. 2023), but an SEE event at energies ≲200 keV was observed by SolO (see Table 1 and Section 4.2). We note that observations of type II radio bursts produced by fast EUV wave fronts ahead of jets, but lacking CMEs, have been previously reported in the literature (e.g., Kumar & Manoharan 2013; Kumar & Innes 2015; Kumar et al. 2016).

With the exception of an additional metric type II radio burst observed between 20:00 UT and 20:15 UT on November 9 at frequencies 180–25 MHz, temporally associated with a C4.3 SXR flare from N28E01 at 19:46 UT (see Table 1), no other metric type II radio bursts were listed in the NOAA/SWPC/SGD reports throughout the time period analyzed in this paper. The association of this metric type II radio burst with the C4.3 SXR flare would imply an origin associated with an EUV jet starting at 19:36 UT (see Table 1). A CME originating from a different region at S27E62 started to propagate over the southeast limb of the Sun at 19:56 UT on November 9 as seen in SDO/AIA 193 Å images and later in WL images by the Large Angle Spectroscopic Coronagraph (LASCO; Brueckner et al. 1995) on board SOHO with a plane-of-sky speed $V_{\rm CME} = 228\,{\rm km\,s^{-1}}$ and plane-of-sky width $\omega_{\rm CME} = 130°$ (as reported in the Coordinated Data Analysis Workshop, hereafter CDAW, catalog of CMEs[28]; Yashiro et al. 2004). This WL CME appeared in the LASCO/C2 coronagraph field of view at 20:24 UT on November 9 with leading edge at the position angle PA = 123° and at a height of 2.42 $R_\odot$ (note that the position angle is measured counterclockwise from solar north in the C2 coronagraph images). This CME is still compatible with the observation times of this metric type II. Regardless of the origin of this metric type II, no SEE event was observed by any of the spacecraft at this time.

3.3. Coronal EUV Jets and Brightenings

Coronal jets, understood as explosive collimated eruptions magnetically rooted on the Sun surface that propagate up into the corona, may display varied morphologies from narrow elongated spires, to large eruptive structures or surges, occasionally with helical or twisted formations (e.g., Moore et al. 2010; Raouafi et al. 2016; Bučík et al. 2018; Shen 2021). Rapid jets may even be accompanied by large-scale propagating EUV waves (e.g., Bučík et al. 2015, 2016; Nitta et al. 2015). On the other hand, EUV brightenings are sudden

[28] cdaw.gsfc.nasa.gov/CME_list/

amorphous increases in EUV light without any clear evidence of material being ejected. The distinction between EUV jets and brightenings could be due to the fact that the ejected material is not bright enough to be detected by current instrument capabilities. However, other factors such as projection effects, the time cadence and wavelength of the observations, or that the magnetic field configuration of these brightenings does not allow the escape of material into the corona, may also play a role in the lack of detection of coronal jets (e.g., Shen 2021). The development of a large-scale coronal front (CF) originating from an EUV jet depends on multiple factors such as the initial speed and size of the driving jet as well as the medium where the jet propagates. The relative speed between the jet and the local Alfvén speed determines whether these CFs are just sub-Alfvénic compressive waves or structures that can steepen into shocks in the case of super-Alfvénic jets that may then act as efficient particle accelerators (e.g., Kozarev et al. 2017; Lario et al. 2017b; Kouloumvakos et al. 2019).

In order to determine whether EUV brightenings, jets, or CFs were observed in association with the SEE events, we have examined SDO/AIA images at the wavelengths 94, 131, 171, 193, 211, and 304 Å together with 195 Å and 304 Å images from the Extreme Ultraviolet Imager (EUVI) of the Sun Earth Connection Coronal and Heliospheric Investigation (Howard et al. 2008) on board STA. The cadence of the SDO/AIA images used was ∼1 minute. For STA/EUVI, the cadence was 5 minutes for 195 Å images and 10 minutes for 304 Å images. Column (5) of Table 1 lists the onset time (with a resolution of 1 minute) of these EUV emissions as observed in SDO/AIA 193 Å images from 2022 November 9 to November 14 (inclusive). We indicate whether the signature of the EUV emission corresponds to a brightening (indicated by the label *B*), a jet when some ejected material can be followed in successive images, or to a CF (indicated by the label *CF*) when the ejected material drove a front seen as a propagating arch in the EUV images. Within the jets class, we have distinguished those cases when the jet is just a narrow small signature with a width of less than a fraction of a degree, from those cases when the jet is a wider structure. Those cases when the wide ejected structure can be tracked by more than ∼10° from its origin are indicated by the label *EJ*. When necessary, additional characteristics of the observed EUV emission are also indicated in column (5) of Table 1. The specific features of these EUV emissions depend to a large extent on the used wavelength, the time cadence of the images, and even the subjective perception of the observer. The timing and the phenomenological descriptions in column (5) of Table 1 are based on ∼1 minute cadence of the 193 Å SDO/AIA images, and these may differ from those inferred using other wavelengths or time cadences.

Column (6) of Table 1 provides the longitude and latitude in Stonyhurst heliographic coordinates (with a resolution of 1°) of the site of either the brightening for the *B* events or the region where the ejected material originated. Most of these EUV jets and brightenings originated at the periphery of the ARs 13140 and 13141 (see for example the case shown in Figure 6). The location of these ARs near central meridian longitudes from November 9 to November 12 facilitated the observation of small brightenings and small jets, with some possible jets appearing just as brightenings due to projection effects. Later, when the ARs were at western longitudes, small events may have been hidden by coronal structures, but the largest EUV emissions, including structures propagating over the west limb, were more easily observed. The associations made in Table 1 with specific X-ray flares listed in columns (1) through (4) are based on their concomitant occurrence and location. The associations made in Table 1 with the electron events listed in column (8) are based on their close temporal occurrence. In the case of consecutive EUV emissions, a one-to-one association between a single solar phenomenon and a single SEE event can be difficult to establish. In particular, linking the most intense SEE events with the most prominent EUV emission can be sometimes misleading since some SEE and ^{3}He-rich events can only be associated with EUV brightenings (e.g., Mason et al. 2023a; Nitta et al. 2023). For this reason, in the next section, we examine the interdependence between the phenomena discussed here (i.e., EUV jets, X-ray flares, type III radio bursts), and the electron SRTs for the observed SEE events.

4. Interdependence between X-Ray Flares, EUV Jets, Type III Radio Bursts, and SEE Events

Figures 7 and 8 show, from top to bottom, (a) the 1 MHz radio intensity in solar flux units (s.f.u.) measured by STA/SWAVES; (b) the 304 Å EUV intensity integrated over a box centered at the coordinates indicated in each panel using measurements from STA/EUVI in Figure 7 and SDO/AIA in Figure 8; (c) ∼75 keV electron intensities measured by the sunward apertures of STA/SEPT (red) and SolO/EPD/EPT (blue); (d) ∼6–10 MeV proton intensities measured by the Low Energy Telescope (Mewaldt et al. 2008) on board STA (i.e., STA/LET) (red) and by SolO/EPD/HET (blue); (e) 1–8 Å SXR intensities detected by the X-ray Sensor (XRS) on board GOES-16 (black),[29] and 15–25 keV HXR count rates provided by SolO/STIX (teal). Each column of Figures 7 and 8 corresponds to a single day from 2022 November 9 to 2022 November 14 (inclusive). The vertical dotted–dashed lines in Figures 7 and 8 indicate the estimated electron release times listed in column (8) of Table 1. Note that the times of the X-ray intensities from GOES and SolO/STIX in panels (e) of Figures 7 and 8 have been shifted back to account for the light transit time from the Sun to Earth and SolO locations, respectively. Similarly, the 304 Å EUV intensity-time profiles in panels (b) have been shifted by the light transit time from the Sun to STA and L1 in Figures 7 and 8, respectively. The 1 MHz radio intensity-time profiles in panels (a) of Figures 7 and 8 have been time shifted by assuming that this emission originated from a height of 8 $R_\odot$ before being measured by STA/SWAVES. The red circles in panels (a) of Figures 7 and 8 indicate the type III radio bursts for which Langmuir waves were detected by STA/SWAVES. These type III radio bursts coincide with the most intense >75 keV electron events shown in Figures 7(c) and 8(c).

The boxes selected to compute the EUV intensities shown in panels (b) of Figures 7 and 8 include the location where most of the prominent EUV jets and brightenings were observed. The coordinates provided in each panel (b) indicate the Stonyhurst position of the center point at the beginning of each day (we also provide its Carrington Longitude (CL) that remains the same throughout the day). The size of the selected box is indicated in units of pixels of the original images (STA/EUI full-size images are 2048 × 2048 corresponding to 1.7″ pixel^{-1}; whereas SDO/AIA full-size images are 4096 × 4096 pixels corresponding to

[29] www.ngdc.noaa.gov/stp/satellite/goes-r.html

$0.6''$ pixel^{-1}). To derive the lightcurves for each day, all the images collected during that day were first derotated using the time of the first image of the day as reference to compensate for the solar rotation. The lightcurves were then obtained by adding the intensity of each pixel belonging to the selected region after subtracting a background image. This background image approximates the intensity of the quiet Sun and is estimated from the median intensity of the bottom 20% intensity in time at each pixel. Therefore, the lightcurves in Figures 7(b) and 8(b) can be considered as normalized integrated 304 Å EUV intensities and are given in units of SDO data number (DN) per second (see details in Ugarte-Urra & Warren 2012; Ugarte-Urra et al. 2015). The EUV intensity enhancements seen in the 304 Å lightcurves of the Figures 7(b) and 8(b) are indicated by the flag E in column (5) of Table 1 (although the identification of the EUV features made in Table 1 is based on SDO/AIA 193 Å images rather than 304 Å images).

For 2022 November 9, we include in panel (b) of Figure 7 an additional EUV intensity-time profile (orange trace) computed over a different area that includes an EUV large-scale slowly rising structure lacking a clear jet that occurred almost simultaneously with the estimated SRT of the low-energy ($\lesssim$45 keV) SEE event (Figure 3) associated with the ion event #1 in Figure 5. This slow-rising structure occurred from a region at a latitude ∼N30 and in longitudes ranging from W17 to W34 (see details in Section 4.3) that was not included in the area used to compute the black EUV intensity curve. At that time, a small EUV brightening was also observed at N24E01 that could be related to this large-scale slow-rising structure (see details in Section 4.3); this small EUV brightening is not captured by the area used to compute the EUV intensity-time profiles in the leftmost panel (b) of Figure 7.

For the ion event #6 at the end of 2022 November 14 (Figure 5), a large-scale confined slow-rising EUV structure occurred at the estimated SRT of the associated SEE event. This structure occupied a large area from W34 to W56 in longitude and at about ∼N10 in latitude at the southeast of AR 13141 (see details in Section 4.3). The area covered to compute the 304 Å intensity-time profile in the rightmost panel (b) of Figure 8 included, in addition to both ARs 13140 and 13414, the area where this large-scale EUV structure rose. However, it only contributed a small increase in the EUV intensity that was followed by a brightening and a jet from AR 13140 that could be associated with the origin of a subsequent low-energy (<58 keV) SEE event at the end of November 14 (see Table 1) .

Figures 7 and 8 display a clear association between SEE release times with intense type III radio bursts, intense HXR flares, and increases in the EUV intensities produced by coronal jets and/or brightenings, especially for the events on November 11 and 12. Notable exceptions include the following:

(1) The sequence of small HXR flares from ARs 13140 and 13141 during the second half of November 9 for which no SEE events were observed. The two GOES C1.2 and C4.3 flares at 17:55 UT and 19:46 UT on November 9 associated with intense EUV jets stand out in this period, but no energetic electron increases were detected in association with these events.
(2) The low-energy ($\lesssim$100 keV) SEE event with SRT at 11:25 UT on November 10 associated with a small type III radio burst and a small narrow EUV jet starting at 11:18 UT (solar time), extending up to 11:21 UT (solar time), but lacking any significant X-ray emission.
(3) The small SEE event with SRT at 19:49 UT on November 10 observed at energies $\lesssim$80 keV associated with a small EUV jet but lacking any jet or clear X-ray emission.
(4) The intense HXR flare and M1.1 SXR flare associated with a continuous EUV eruption at 00:04 UT (solar time) on November 12 for which no type III radio bursts and no new SEE intensity increase were observed.
(5) The long-duration SXR emissions starting at ∼14:50 UT and ∼16:20 UT on November 12 associated with EUV brightenings in footpoints of loops in AR 13141, with no clear EUV jets, concurrent with very weak HXR flares, and for which no increases of electron intensities above ∼10 keV were detected. In contrast, the subsequent sequence of three consecutive SEE events (with increasing maximum energy) occurring after ∼17:00 UT associated with intense EUV emissions, especially the last EUV jet at 17:53 UT (solar time) that drove a CF, a CME, and associated with an intense HXR flare, a C6.5 SXR flare, and an intense type III radio burst.
(6) The intense HXR flare and concomitant GOES C4.0 flare at 06:17 UT on November 13 accompanied by a large EUV jet that developed into a CF, but no type III radio burst or SEE event were observed (see Section 4.2).
(7) The X-ray flares in the last ∼6 hr of November 13 and throughout November 14 located at far western (>W45) longitudes on the Sun as seen from Earth. Many were associated with faint type III radio bursts, but no SEE events at energies above ∼10 keV were observed by SolO. During this period, an EUV brightening at 02:36 UT was followed by two EUV eruptions at 02:39 UT and 02:54 UT on November 14 from longitudes around ∼W34 at the eastern edge of AR 13145 (this AR resulted from the decay of AR 13140, which started to break apart). These eruptions were most likely the origin of the intense SEE events early on November 14 for which two injections were observed at SRT = 02:37 UT and SRT = 02:56 UT that resulted in the ion event #5 in Figure 5 also observed by STA and L1, and also a >25 MeV proton intensity increase at SOHO (see Figure A1).
(8) The ion events #1 and #6 early on November 9 and late on November 14 (Figure 4(d)) observed just at electron energies below ∼45 keV and ∼58 keV, respectively, were not associated with a clear EUV jet or X-ray flare. The solar origin of these two events is analyzed in Section 4.3 below.

Regarding the association made between the onset times of the solar emissions and the SRTs of each SEE event listed in Table 1, we note that there could be some inconsistency, in part due to the uncertainties in the estimated SRTs, but also due to a possible delay between the onset of the solar phenomena and the release of SEEs (e.g., Krucker et al. 1999; Haggerty & Roelof 2002; Kouloumvakos et al. 2015). Figure 9(a) shows the distributions of time delays between the onset of the associated EUV emission for the SolO SEE events observed at energies >10 keV (gray histograms) and the SolO SEE events observed at energies >65 keV (black histograms). Figure 9(b) shows the same time delay distributions but with respect to the onset of the associated HXR flares. For completeness, Figure 9(c) shows the distribution of time delays between the SRT of the SEE events and the estimated onset time of the type

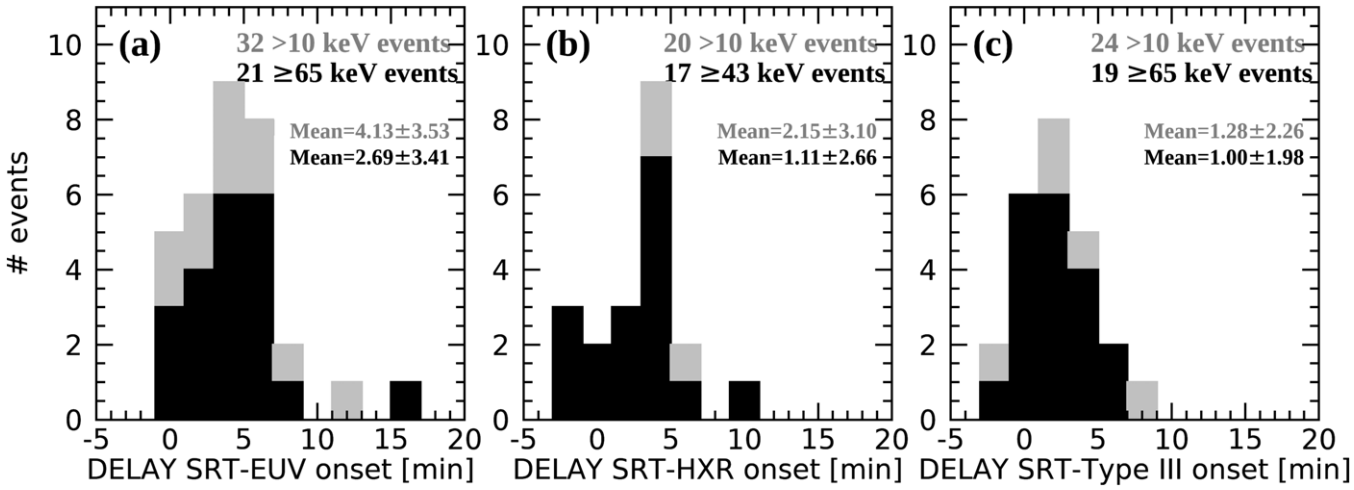

Figure 9. Distributions of the time delays between electron SRTs and the onset of the associated (a) EUV emissions, (b) HXR flares, and (c) type III radio bursts as listed in Table 1. The times listed in Table 1 have been rounded to 1 minute resolution, and the bins used in the histograms are 2 minute wide. The gray (black) histograms are for >10 keV (>65 keV) SEE events observed by SolO. Positive delays indicate that the estimated SRT occurred after the onset of the associated (a) EUV emission, (b) HXR flare, and (c) type III radio burst.

III radio bursts as listed in columns (7) and (8) of Table 1 (note that the type III radio bursts associated with the ion events #1 and #6 that started at low frequencies are not included in Figure 9(c)). The estimated electron SRTs show a delay with respect to the onset of the EUV emission ranging from ∼1 to ∼15 minutes. Such a delay may result from the fact that the electron injection does not occur at the onset of the EUV emission but at a later time, which may correspond to the time when the EUV emission intensifies, when the jet expands a certain distance and encounters open field lines, or compression waves or shocks develop that are able to accelerate particles. Alternatively, if the electrons are only accelerated at the site origin of the jet or the EUV brightening, the electron SRT delay may represent the time needed for the electrons to reach open field lines and escape into interplanetary space. The SEE event with the longest delay of ∼15 minutes had SRT = 13:00 UT on November 13, was observed at energies $\lesssim$102 keV, and was associated with a jet able to drive a CF and a CME (see Section 4.2). The SEE event with the second largest delay (i.e., ∼12 minutes) had SRT = 07:38 UT on November 12 but was observed only by SolO/EPD/STEP at energies below ∼20 keV, which also increases the uncertainty in the SRT. Despite the uncertainties in the SRT times, Figure 9(a) shows a systematic delay in the SRT with respect to the onset of the EUV emission with a mean of ∼4 minutes for >10 keV SEE events and ∼2.7 minutes for >65 keV SEE events.

For those events, with which we have associated an HXR flare, there are also delays between the onsets of the HXR flare and the SRTs (Figure 9(b)), but these are shorter than the delays with respect to the onset of the EUV emissions. Note that the higher the energy reached by the SEE event, the more likely it is to find an association with an HXR flare. For example, it was not possible to find an associated HXR flare for 37.5% of the 32 >10 keV SEE events, compared with 19% of the 21 >65 keV events. This is consistent with prior results for the high-energy (>1.3 MeV nucleon^{-1}) ^{3}He-rich events analyzed by Reames et al. (1988). Owing to the uncertainties in the estimated SRT, there are three cases for which the estimated SRT occurred earlier than the onset of the HXR such as the SEE events with SRT = 09:36 UT and SRT = 11:28 UT on November 11 with delays of ∼−3 minutes. The longest positive delay occurred for the event with SRT = 13:00 UT on November 13 associated with an EUV CF and a WL CME for which the onset of the HXR flare occurred ∼10 minutes earlier (see Section 4.2).

An association with type III radio bursts for which we were able to compute their onset time at 1 $R_\odot$ could be made for 24 out of the 32 >10 keV SEE events and for 19 out of the 21 >65 keV SEE events. The higher the energy reached in the SEE event, the clearer the association with an intense type III radio burst. The delays between SRT and the onset of type III radio bursts are smaller than for the onset of the EUV and HXR emissions. The delay observed, in some events, indicates that the low-energy electrons responsible for the type III radio bursts are apparently released earlier than the SEEs. Uncertainties in the SRTs (Section 2) and type III onsets (Section 3.2) may affect these results, including two events for which the SRT is prior to the type III onset. Note that the type III radio burst onset times were computed under the assumption that they were generated by fundamental emission. If the type III radio bursts resulted from harmonic emission, the inferred type III onset times would have shifted to later times by the order of a few (∼20) s. This would imply a shorter time difference with respect to the energetic electron SRTs, but within the uncertainties used in Figure 9(c).

Delays observed between the SRT and several solar phenomena have been previously discussed in the literature (e.g., Haggerty & Roelof 2002; L. Wang et al. 2006) and have been attributed to the delayed acceleration of electrons by shocks driven by CMEs (e.g., Simnett et al. 2002) and/or scattering transport processes and energy-dependent injection processes leading to errors in SRT estimates (e.g., Kahler et al. 2005, 2007; Ragot & Kahler 2008). In addition, the TSA assumption of scatter-free transport may lead to short SEE travel times and hence delayed SRTs compared to the case when scattering occurs. Similarly, the assumption of a Parker spiral path length may lead to delayed SRTs compared to the case when the actual path followed by the particles is longer. The SRTs may also be impacted by difficulties in identifying SEE onset times due to limited pitch-angle coverage and

closely spaced events. Nevertheless, the observed delays are consistent with prior results (e.g., Haggerty & Roelof 2002; Kouloumvakos et al. 2015), with a trend to shorter delays considering the impulsive nature of the events analyzed here.

Table 1 lists multiple cases of EUV eruptions and X-ray flares without any associated SEE event. Several factors might account for this. Open field lines that would allow the particles to escape may not be present near a particular jet or X-ray flare, or overlying close field lines may impede particle escape. There may also be a lack of magnetic connection between an observing spacecraft and the source of an SEE event, as explained further in Section 4.1. In Section 4.2, we also consider the possibility that the jets were accompanied by large-scale coronal structures able to accelerate and inject SEPs into regions of interplanetary space not necessarily connected to the site where EUV emissions originate. Finally, in Section 4.3, we analyze two confined EUV eruptions that could be associated with the origin of the ion events #1 and #6 identified in Figures 4 and 5.

4.1. Magnetic Connectivity Spacecraft–Sun

An important factor in the detection of SEPs by a spacecraft in interplanetary space is the magnetic connection established between the spacecraft and the particle source (e.g., Lario et al. 2017a, and references therein). Table 1 lists the locations of the flares, EUV brightenings, and the origin of the EUV jets observed throughout the time interval under study. These locations indicate the sites where presumably the acceleration and release of particles started, especially if these processes involved reconnection between close and open field lines offering the opportunity for the accelerated particles to escape into open interplanetary space. In order to estimate the site on the solar surface where a spacecraft establishes magnetic connection, a series of approximations and assumptions regarding the topology of the magnetic field in the corona and in interplanetary space are required. Several methods have been applied in the literature to compute the magnetic connection of spacecraft with the Sun (e.g., Nolte & Roelof 1973; MacNeice et al. 2011; Lario et al. 2017a; Rouillard et al. 2020; da Silva et al. 2023). Common assumptions include a nominal Parker spiral to describe the large-scale configuration of the interplanetary magnetic field and the use of the potential field source surface (PFSS) model (e.g., Schrijver & De Rosa 2003) to describe the coronal magnetic field below the source surface (where the magnetic field is assumed to be radial, usually placed at $2.5\,R_{\odot}$). Here, we use PFSS coronal magnetic field solutions to trace field lines from the Parker spiral field line footpoint on the source surface for each location (SolO, STA, and L1). The tracing is performed in a narrow region of $2.^{\circ}5$ around the Parker spiral footpoint at the source surface. The Parker spiral footpoint is obtained using the solar wind speed measured by each spacecraft (SolO, STA, and ACE) at a specific time. For SolO, there are a few time intervals when solar wind measurements were not available (see Figure A1(f1)). For the solar wind data gaps on November 14, we interpolated the solar wind measurements at nearby times. For the time interval prior to November 11, we assumed a linear decay of the solar wind speed from $600\,\mathrm{km\,s^{-1}}$ at the beginning of November 9 to the actual value observed at the beginning of November 11. For the input to the PFSS model, we utilized the Air Force Data Assimilative Photospheric Flux Transport (ADAPT; Arge et al. 2010) photospheric magnetic field maps based on the Global Oscillation Network Group (GONG) magnetograms.[30] ADAPT is an ensemble model that provides maps using 12 different realizations, with each realization yielding slightly different connectivity (da Silva et al. 2023). Specifically, to estimate the spacecraft magnetic footpoints, we used the realization number 10. The ADAPT maps have a 2 hr cadence, and we selected the map closest to the time used to determine the connection points.

The cross symbols in Figure 10 indicate the heliographic longitudes (top panels) and latitudes (bottom panels) of the magnetic connection points computed at the times of the HXR flares listed in Table 1 using the method described above (hereafter the Parker-PFSS-ADAPT, or PPA method) for SolO (left column), STA (middle column), and L1 (right column). For each single time, the points used in the initial $2.^{\circ}5$ wide region at the source surface tend to converge into one, two, or even three areas on the solar surface as they are tracked down using the PFSS configuration applied to specific ADAPT maps. Rather than assigning the coordinates of the footpoint to the average of the connectivity footpoints obtained from this initial distribution of points, we have plotted in Figure 10 the coordinates of the centroid of each cluster of footpoints computed as that point that minimizes the sum of squared distances between data points and their respective cluster centroids (i.e., using a K-means clustering analysis; Lloyd 1982). The distance between the clusters of points provides an estimate of the uncertainties of the footpoint locations obtained by the PPA method. Figure 10(a1) shows three tracks of footpoint longitudes (crosses in different blue tones) that indicate the longitude of the centroids of the areas where the footpoints accumulate. The footpoint longitudes move toward the west limb, whereas their latitudes (Figure 10(b1)) stay approximately in the same position. The shaded blue areas in Figures 10(a1) and (b1) highlight the clusters of footpoints at similar longitudes that evolve together in time allowing a visual association between the longitude and latitude of each cross symbol. Similarly, Figure 10(a2) shows four tracks of footpoint longitudes (crosses in different red tones) for STA, although for each single time there are just one, two, or three clusters of footpoints. The reddish crosses in Figure 10(b2) indicate the latitudes of the centroids of the cluster of STA footpoints. The shaded pink areas associate the longitude and latitude of those footpoints at similar longitudes that evolve together with time from east to west. Note that on November 14 a cluster of footpoints accumulated at longitudes in the range W45–W60 and latitudes N12–N13. Finally, Figure 10(a3) shows three tracks of footpoint longitudes (crosses in different green tones) for spacecraft at L1, whereas the greenish crosses in Figure 10(b3) indicate their latitudes. Note that during November 14 two clusters of footpoints were obtained at longitudes in the ranges W45–W60 (with latitudes within N08 and N13) and W90–W105 (with latitudes N17–N35).

The blue solid lines in Figures 10(a1) and (b1) indicate the longitude and latitude of the SolO magnetic footpoint using just the nominal Parker spiral considering the same solar wind as when computing the connection footpoint using the PPA method. Similarly, the red solid lines in Figures 10(a2) and (b2) and the green solid lines in Figures 10(a3) and (b3) indicate the

[30] gong.nso.edu/adapt/maps/

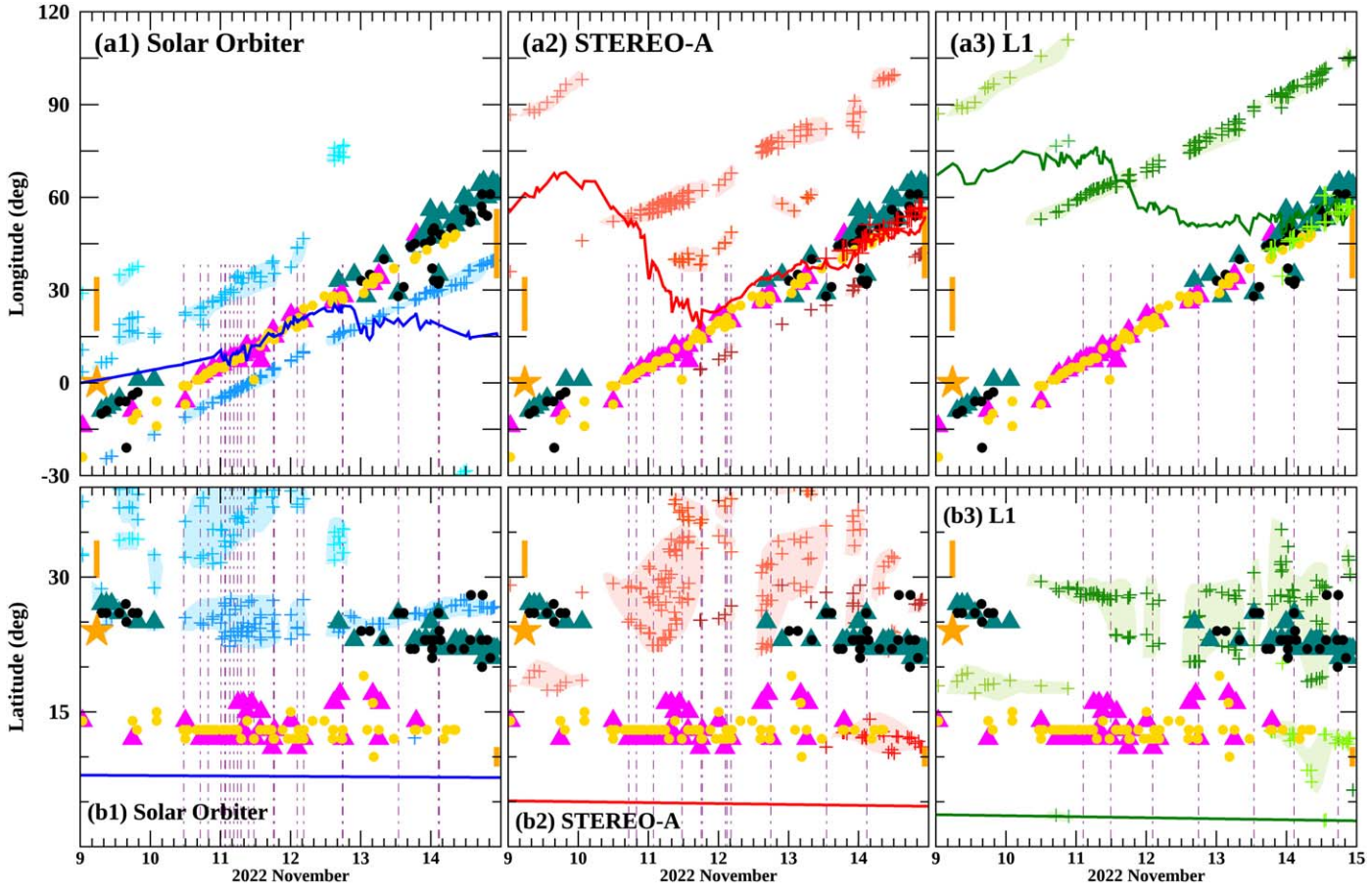

Figure 10. Heliographic coordinates of the HXR flares observed by STIX (magenta and teal triangles), EUV jets/brightenings (small orange and black circles), and of the magnetic connection points of, from left to right, SolO (blue symbols), STA (red symbols), and L1 (green symbols) estimated using the Parker-PFSS-ADAPT (PPA) method (crosses) or just a Parker spiral configuration (solid lines). Magenta (teal) triangles indicate when the HXR flare occurred in AR 13141 (AR 13140). Small orange (black) circles indicate when the EUV jets and/or brightenings occurred in the vicinity of AR 13141 (AR 13140). The vertical dotted–dashed lines indicate the SRT of the >65 keV SEE events observed by SolO (left column), STA (middle column), and Wind (right column). The shaded areas highlight the clusters of footpoints at similar longitudes that evolve together in time as obtained by the PPA method.

coordinates of the footpoints of the nominal Parker spiral field lines connecting to STA and L1, respectively.

Several factors play a role in the accuracy of the estimated footpoint locations plotted in Figure 10. First, the field configurations assumed in both the PPA and the Parker spiral methods may differ from the actual field configurations. For example, the high-speed solar wind stream (HSS) and an SIR sequentially observed by SolO, STA, and near-Earth spacecraft (see Appendix A) may have distorted the interplanetary field configuration from a nominal Parker spiral. In particular, the magnetic field tends to be more radial in the rarefaction region of an HSS (e.g., Murphy et al. 2002; Lario & Roelof 2010), and the interaction of slow and fast solar wind in the SIR may distort the magnetic field. Deviations of $\sim 10^{\circ}$ when using Parker spiral ballistic backmapping from 1 au are expected to occur (Nolte & Roelof 1973), whereas different assumptions for acceleration and corotation of the solar wind also introduce variations in the estimated footpoint locations (e.g., Dakeyo et al. 2024, and references therein). Magnetic field meandering in interplanetary space may also lead to deviations in the assumed nominal Parker spiral field lines (Giacalone & Jokipii 2004). Additionally, the PFSS configuration assumed in the PPA method may not be an accurate representation of the coronal magnetic field. It is well known that the choice of magnetogram used for input as well as the ADAPT realization selected may provide different connectivity results (e.g., Lario et al. 2017a; da Silva et al. 2023). Also, the potential field assumption made in the PFSS model does not incorporate time-dependent phenomena such as magnetic reconnection or the effects produced by propagating coronal jets frequently observed in the period under study, nor the rapid changes in the low corona that may have occurred. Therefore, a precise estimate of the uncertainties of the footpoint locations displayed in Figure 10 is difficult to evaluate, and the plotted values should be judiciously considered.

The magenta and teal triangles common to each panel of Figure 10 indicate the coordinates of the HXR flares obtained from STIX observations, whereas the orange and black circles indicate the location origin of the EUV jets and/or brightenings indicated with the flag E in column (5) of Table 1. The magenta triangles and orange circles are used when the HXR and the EUV emissions occurred near AR 13141, whereas the teal triangles and black circles indicate if they occurred near AR 13140. Figure 10 shows the close concomitance in time and location between the HXR (triangles) and EUV (circles) emissions. At the beginning of the time interval under study (November 9) and at the end (from mid-November 13 and throughout November 14), most of the emissions occurred near

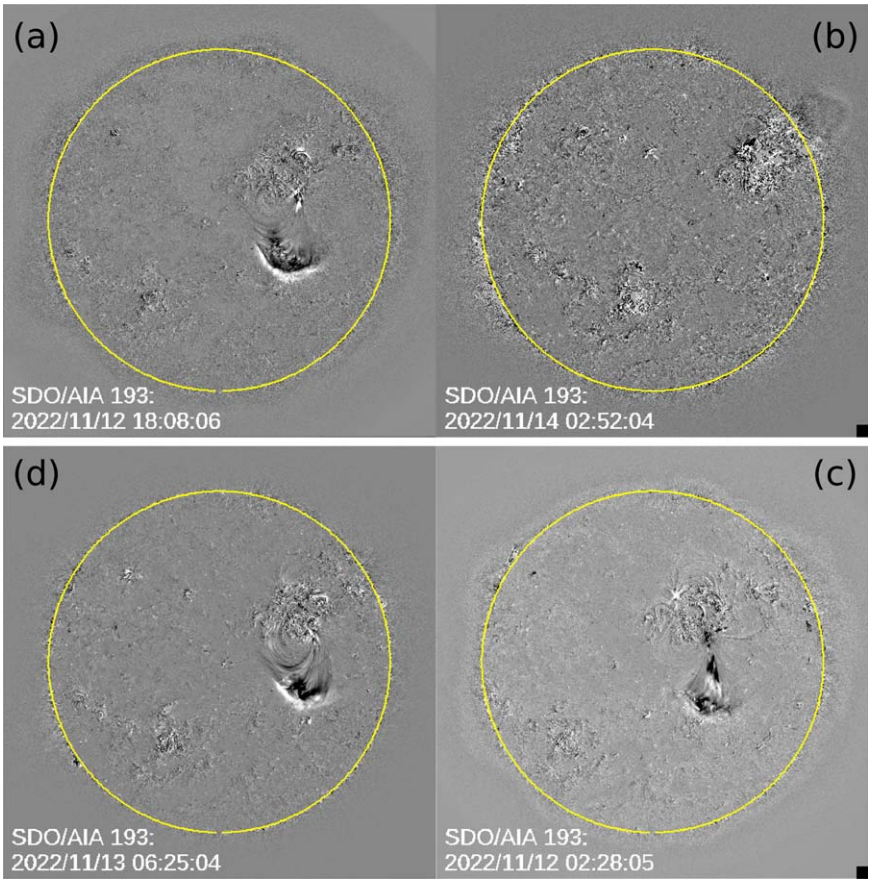

Figure 11. SDO/AIA 193 Å running difference images shortly after the origin of the ion events #4 (a), #5 (b), and #3 (c) as identified in Figure 5. The solar eruption and CF in panel (d) was not associated with any particle event. The eruptions in panels (a) and (b) were associated with white-light SOHO/LASCO CMEs. No white-light CMEs were identifiable in association with the eruptions in panels (c) and (d).

AR 13140, whereas throughout November 10, 11, and 12 most of the activity occurred near AR 13141. Figure 10 includes also an orange star symbol early on November 9 at N24E01 that indicates the location of a small EUV brightening probably associated with the low-energy ($\lesssim$45 keV) SEE event and ion event #1 (see Section 4.3). The orange bars occupying (i) the longitudes and latitudes W17–W34 and N30–N34 early on November 9, and (ii) W34–W56 at N10 late on November 14 indicate the location of large-scale slow-rising confined EUV structures lacking a clear EUV escaping jet that could be associated with the ion events #1 and #6 and the associated SEE events (see details in Section 4.3).

Figure 10 shows that, within the uncertainties described above, the footpoints of the nominal Parker spiral field lines connecting to SolO were close in longitude to the site of the solar eruptions on November 11–12, but separated in latitude by $\sim$7°. By contrast, the footpoints computed using the PPA method during the same period were separated by $\sim$10° in longitude, and more than $\sim$10° in latitude. For STA (L1), the nominal Parker spiral footpoints were close in longitude to the site of the solar eruptions from November 12 (14) onwards, but the latitudes were separated by more than $\sim$10°. Note that, for the PPA method, STA and L1 footpoints were close to the site of the solar eruptions on November 14, but this is not the case for SolO.

Despite the uncertainties in the connectivity computations, Figure 10 shows that, except for STA and L1 PPA footpoints on November 14, there was a large ($\gtrsim$10°) distance between the estimated footpoint locations and the site where the EUV jets and brightenings originated. This is especially problematic for the observation of particles if their sources were limited in extent, and SEE release occurred only where EUV brightenings and jets originated. The cases of extended jets able to generate CFs, or even expand to higher altitudes driving CMEs, may offer the possibility to create coronal disturbances that may accelerate energetic particles over a broad range of latitudes and longitudes (e.g., Kozarev et al. 2017). In the next section, we describe whether these structures (CFs and CMEs) were observed in association with the release of SEEs, and whether they propagated toward the sites of the estimated magnetic connection footpoints.

4.2. CFs and CMEs

Figure 11 displays SDO/AIA 193 Å running difference images observed shortly after the onset of some of the largest EUV jets listed in column (5) of Table 1. Three of these jets (panels (a), (c), and (d)) were able to drive CFs. The CF in Figure 11(a) was driven by a jet that was observed to originate at $\sim$18:01 UT on November 12 from N13W27. According to the CDAW/SOHO/LASCO CME catalog, a WL CME with a plane-of-sky speed $V_{\rm CME} = 175$ km s^{-1} and plane-of-sky width $\omega_{\rm CME} = 45°$ appeared in the LASCO/C2 coronagraph field of view at 19:12 UT on November 12 with leading edge at PA = 241° and at a height of 2.54 $R_\odot$. It is likely that this CME

originated with the jet that drove the CF shown in Figure 11(a). However, its origin close to central meridian (as seen from Earth) makes the observation of the CME difficult with V_{CME} and ω_{CME} values significantly influenced by projection effects.

The CF shown in Figure 11(c) was driven by a jet that was observed to originate at 02:19 UT on November 12 from N13W32. In this case, no clear WL CME was seen in LASCO images, nor can any material expelled over the limb of the Sun be seen in EUV images that could be associated with this jet. Similarly, the CF in Figure 11(d), driven by a jet originating at 06:18 UT on November 13 from N13W34, did not show any trace of ejected material over the solar limb in either EUV or WL images. By contrast, the eruption in Figure 11(b) started as an EUV brightening at 02:44 UT on November 14 that was followed by an extended jet observed at 02:47 UT moving mostly in the vertical direction. This did not leave any clear signatures close to the solar surface in the form of an EUV wave or CF, but extended to higher altitudes in the form of a CME (seen both in EUV and WL images). In fact, a narrow CME can be seen in Figure 11(b) over the west limb at PA $\sim 290°$ that appeared later in the LASCO/C2 field of view with leading edge at $2.9\,R_{\odot}$ at 03:24 UT. According to the CDAW/SOHO/LASCO CME catalog, this CME had a plane-of-sky speed $V_{CME} = 321\ km\ s^{-1}$ and width $\omega_{CME} = 74°$.

The jet origin of the CF in Figure 11(a) was associated with (i) an SEE event clearly seen at all three locations (SolO, STA, and L1) even at relativistic energies (indicated by the first green circle in Figure 2(c)), (ii) a $\gtrsim$7 MeV proton intensity increase at the three locations (Figure A1), and (iii) the ion event #4 in Figure 5. The jet origin of the CF in Figure 11(c) was associated with (i) an SEE event clearly observed by STA and SolO (although the event at SolO only reached energies $\lesssim$200 keV) and (ii) the ion event #3 in Figure 5. Note that this SEE event was followed by a more intense SEE event at SolO with estimated SRT at 04:28 UT that probably originated with a jet at 04:25 UT (solar time) on November 12 which was able to drive a CF (not shown here) though no material was evident over the limb in WL or EUV. The sequence of two SEE events at energies $\lesssim$300 keV was observed also at STA and L1 (see Figures 2(b), A1(a2), and (a3)), whereas at energies $\gtrsim$2.5 MeV the intensity increases observed by SOHO/EPHIN early on November 12 (second open green circle in Figure 2(c)) could be related to the jet at 04:25 UT, but no clear CME (either in EUV or WL images) could be associated with it. Note that, according to Hou et al. (2023), the jet at 02:19 UT (02:11 UT solar time) on November 12 that was the origin of the CF in Figure 11(c) was able to drive a shock responsible for a metric type II radio burst. However, the estimated Alfvén Mach number of this shock was only in the range 1.09–1.18, implying a weak shock. Therefore, the gradual relativistic SEE intensity increase observed at L1 early on November 12 was most likely associated with the jet at 04:25 UT (solar time), but for which no CME was observed.

Figure 11(d) displays another CF observed during this period that was associated with an intense HXR flare (see Figure 8), but for which we could not associate any SEP intensity increase. We note that all the CFs identified moved southward (as those shown in Figures 11(a), (c), and (d)) and were limited in extent because of the neighboring CHs (Figure 6). Additionally, the CFs moved in the opposite direction of the northern latitudes where the estimated footpoints of field lines connecting to the spacecraft were located (Figure 10). It is possible that the jets moved vertically, being able to compress or even drive shock waves propagating at higher altitudes that intercepted the field lines connecting to the spacecraft. However, these jets did not leave a clear trace on the northern part of the solar disk that could be detected in EUV images. Noticeably, the observation of a CF, such as the one shown in Figure 11(d), did not warrant the observation of an SEP event.

The eruption in Figure 11(b) with the 321 km s^{-1} WL CME over the west limb was associated with the origin of the ion event #5 in Figure 5 and the intense SEE event observed by the three spacecraft early on November 14 (see Figure 2). However, it did not display a clear CF over the solar disk. The SEE event could have started with an EUV brightening at 02:44 UT on November 14 and continued with the extended jet at 02:47 UT but only reaching energies $\lesssim$237 keV at SolO. By contrast, this SEE event was observed at relativistic energies by SOHO/EPHIN (indicated by the third green circle in Figure 2(c)). In fact, this SEP event was observed even at proton energies $\gtrsim$25 MeV by SOHO/COSTEP/EPHIN (Figure A1(b3)) and as a ^{3}He and Fe-rich event by ACE/ULEIS. The largest intensities and higher energies of this event at L1 may be a consequence of the better magnetic connection to the source region for near-Earth spacecraft than for SolO (Figure 10).

For completeness, we should indicate that, during the period under study, the CME with the fastest plane-of-sky speed reported in the CDAW/SOHO/LASCO CME catalog was an extremely narrow CME with $\omega_{CME} = 9°$, $V_{CME} = 560\ km\ s^{-1}$, and PA = 268° at 02:36 UT on November 14 that cannot be associated with any EUV event occurring on the visible side of the Sun. The widest CME during this period appeared in the LASCO/C2 field of view at 09:12 UT on November 11 with $\omega_{CME} = 139°$ and $V_{CME} = 190\ km\ s^{-1}$. This CME was most likely generated from behind the west limb of the Sun as seen from Earth, and no SEP event could be associated with it.

In column (5) of Table 1, we indicate when a CME or material expanding over the solar limb could be observed. Apart from the two cases shown in Figures 11(a) and (b), we should add the following:

1. A CME observed by LASCO/C2 at 13:36 UT on November 13 with $V_{CME} = 397\ km\ s^{-1}$ and $\omega_{CME} = 85°$ at PA = 320° probably associated with the EUV jet at 12:53 UT from N26W28. This CME was most likely associated with an SEE event at SolO measured at energies $\lesssim$102 keV, but at even higher energies and with higher intensities at STA and Wind (see Figures 2(a)–(b)). Of note is that this SEE event was even measured at energies above ~2.64 MeV by SOHO/COSTEP/EPHIN (indicated by the second green circle in Figure 2(c)). The SEE event at SolO showed a delay of ~15 minutes between the estimated SRT and the origin of the EUV jet, whereas for Wind the delay was of ~6 minutes, which may be due to the time required for the jet to drive a shock with a better connection to L1 than to SolO.
2. A CME observed by LASCO/C2 at 18:42 UT on November 14 with $V_{CME} = 278\ km\ s^{-1}$ and $\omega_{CME} = 64°$ at PA = 285° probably associated with the EUV jet at 17:59 UT from N28W55. The associated SEE event (see Figures 2(a)–(b)) was observed at L1 but not at STA or SolO (presumably L1 was much better magnetically connected; see Figure 10).

3. Material expanding over the west limb of the Sun seen in both EUV and WL images, probably associated with the EUV jets at 09:27 UT and 17:39 UT on November 14 that extended into the WL C2 coronagraph images seen at 10:24 UT at PA = 260° and at 18:42 UT at PA = 290°, respectively. This amorphous ejected material was not even classified as a CME in the CDAW/SOHO/LASCO CME catalog. We indicate these two jets with CME* in column (5) of Table 1. None of these two jets could be associated with SEE events.

Apart from these three items above, no other WL CME reported in the CDAW/SOHO/LASCO CME catalog or any other WL material seen in LASCO/C2 images seem to be associated with the origin of the observed SEE events. Also, since the observation of CMEs generated by these jets is facilitated when the source of these jets is close to the limb (rather than close to central meridian longitudes), most of the WL CMEs were observed late on November 12, and during November 13 and 14.

4.3. The Solar Origin of the Ion Events on 2022 November 9 and November 14

Table 2 shows that the events associated with heavy-ion intensity increases tend to be associated with jets able to drive CFs. Two significant exceptions are the ion events #1 and #6 in Figure 5 that were very prominent at low-energy ($\lesssim$1 MeV nucleon^{-1}) ion intensities but for which electron intensity enhancements only reached energies below ~45 keV and ~58 keV, respectively (see Figures 4, 5, and 3(a)). The type III radio bursts associated with these events were observed only at low frequencies (see Figure 3(b)).

For the ion event #1, two EUV episodes occurred almost simultaneously that were coincident with the estimated electron SRT but far from the two ARs (see Table 1). Figure 12(a) shows an SDO/AIA 211 Å image of the region where the two EUV episodes took place prior to their occurrence. The overplotted white and black contours indicate regions of strong (~100 G) positive (white) and negative (black) polarity line-of-sight magnetic field as measured by the Helioseismic and Magnetic Imager (HMI; Scherrer et al. 2012) on SDO. An inverse S-shaped filament channel (indicated by the white arrow) can be seen northwest of the main positive magnetic region. Figures 12(b) and (c) are SDO/AIA 211 Å running difference images displaying the structures associated with these two EUV episodes. The two red arrows labeled N30W17 and N33W34 indicate the coordinates of the footpoints of the inverse S-shaped filament as it developed as a confined slow-rising structure. At ~05:20 UT, some material was seen moving along the filament toward its western foot. The whole structure increased in size at ~05:36 UT, and started to rise at ~05:45 UT, reaching a maximum extent at ~06:03 UT, and then decaying until around ~06:46 UT. Throughout this evolution, there was no observational evidence of material being ejected from this structure. The confinement of this structure was most likely due to the effects produced by overlying magnetic field, in such a way that brightenings on this slowly rising structure resulted from interactions with the material above, and any possible jets would have remained confined by upper coronal loops. Material moving along this slowly rising structure may precipitate in the footpoints of the filament producing brightenings (Wyper & DeVore 2016; Kumar et al. 2019a). Coincident with the expanding of this slowly rising structure, a brightening at N24E01 (left red arrow in Figure 12(b)) occurred, with bright material running along a pre-existent close loop, but again with no evidence of ejected material. An additional small jet observed at 06:01 UT (or 05:53 UT in solar time) from the western edge of AR 13141 at N12E17 (not included in Figure 12) seems to occur too late to explain the low-energy SEE event with SRT = 05:47 UT, but is still compatible with the onset of the ion event #1 (Table 2). No X-ray flaring emission was observed in association with all these EUV episodes. Whether the low-energy $\lesssim$45 keV electrons and $\lesssim$1 MeV nucleon^{-1} ions observed during this SEP event were released from the EUV brightening close to central meridian, the large-scale rising structure, or the later small jet, cannot be resolved. The estimated magnetic field connectivity for SolO favors the small brightening close to central meridian (see orange star in Figures 10(a1)–(b1)). However, the largest EUV phenomenon occurring at this time was the western slowly rising structure although this was distant from the estimated SolO magnetic connection (left orange bar in Figures 10(a1)–(b1)).

In order to explain the ultraheavy-ion intensity enrichment observed in this ion event #1, Mason et al. (2023b) invoked a particle acceleration mechanism consisting of preferential heating via interaction of electromagnetic hydrogen cyclotron waves with a seed population of different ion species (Roth & Temerin 1997). Heavy ions are resonantly accelerated by the second or higher harmonics of these waves, whereas the most abundant ^{4}He and H ions damp the waves at the frequencies resonant with these particles. The background magnetic field gradient is an important component of this acceleration process, wherein the magnitude of the acceleration is proportional to the field gradient. Owing to the field gradient, particle cyclotron radii changes along this gradient allow a single wave to accelerate particles with a range of cyclotron frequencies. This process leads to an increase in the Fe/O ratio due to a depletion of O (see details in Mason et al. 2023b). It is possible that this field gradient can be found in coronal loops or as the large-scale structure rises to higher coronal altitudes where enhancements of low first-ionizing-potential elements (such as Fe) in closed field structures have been observed (e.g., Mondal et al. 2023). However, the mechanism allowing the release of particles onto open magnetic field lines from these closed structures remains uncertain. One possibility is that interchange magnetic reconnection processes at the footpoints of these structures where brightenings occur enable the particles to find open field lines and hence the possibility to escape toward interplanetary space, or alternatively, this reconnection may occur at higher altitudes explaining the weak or inexistent signatures of the type III radio burst at high frequencies.

The right column of Figure 12 shows SDO/AIA 211 Å images of the region where most likely the ion event #6 originated. Figure 12(d) shows an SDO/AIA 211 Å image at the time of the estimated electron SRT. The SDO/HMI ± 100 G line-of-sight magnetic field contours concentrated where ARs 13141 and 13140 were located (top right corner of the figure). The white arrow identifies a filament structure that extends from the position indicated by the arrow to the southwest edge of the white magnetic field polarity at the center of the image. The filament started to rise at around ~22:31 UT with material moving downward

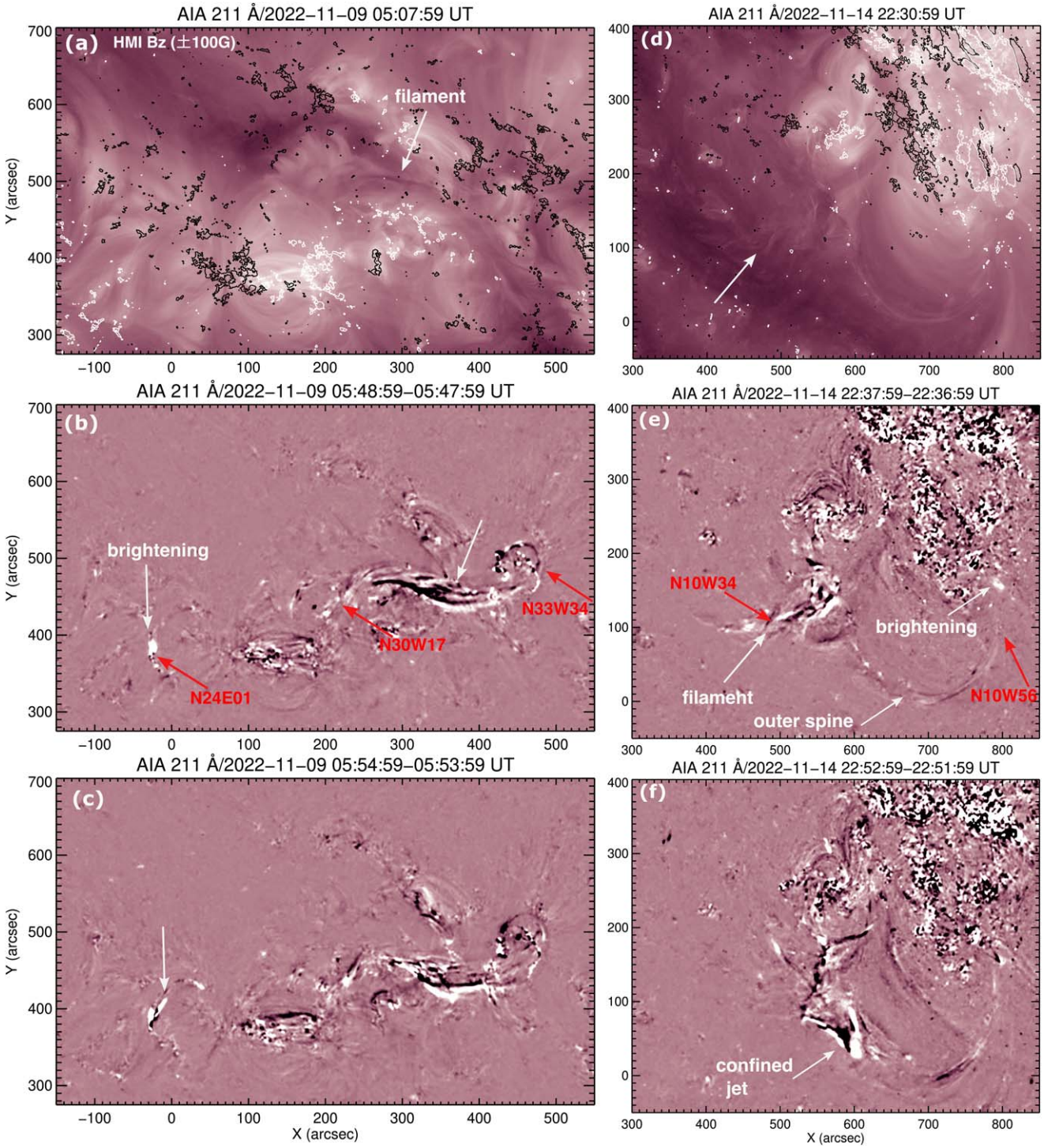

Figure 12. SDO/AIA 211 Å images for the EUV phenomena related to the origin of the ion events #1 (left column) and #6 (right column). The top two panels are direct SDO/AIA 211 Å images prior to the estimated SRTs of the associated SEE events, with overlaid SDO/HMI line-of-sight magnetic field polarity (white and black contours). The four bottom panels are running difference images indicating the main features associated with these EUV confined eruptions.

toward N10W34 (left red arrow in Figure 12(e)) whereas other material moved toward the western footpoint at N10W56 (right red arrow in Figure 12(e)) along a closed structure (identified as outer spine in Figure 12(e)). A confined jet indicated in Figure 12(f) was also seen to propagate along this structure. The continuous motion of material along this closed structure ended at ∼23:45 UT but without displaying any clear evidence of material ejected to higher altitudes.

Figure 12 shows the largest EUV phenomena occurring over the whole solar disk at the estimated SRT times of the low-energy SEE events associated with the ion events #1 and #6. No X-ray flaring emission was observed at those times. Whereas the slow-rising confined structures are similar for the two events, the ion event #6 displayed smaller Fe/O and ^{3}He/^{4}He ratios than the ion event #1 (Table 2), whereas ultraheavy-ion intensity enrichments were only observed in the ion event #1 (Mason et al. 2023b). The similarity between the

two SEE events lies in the fact that the electron intensity enhancements were observed just at low energies (i.e., below ~50 keV) and that the associated type III radio bursts started at low (<1 MHz) frequencies. Probably, overlying closed field configurations inhibited the release of clear EUV jets into open space and hence the escape of an intense electron beam able to generate a strong radio emission from low in the corona. A continuous leakage of particles from adjacent open field lines, probably during brightenings produced by interchange reconnection, could be at the origin of these two low-energy particle events, and only at larger distances was the beam of electrons intense enough to generate type III radio emission.

5. Discussion

The intense series of SEE events observed by SolO, STA, and L1 spacecraft from 2022 November 9 to November 15 offers the possibility to analyze the association between the release of energetic electrons and solar EUV brightenings, EUV jets, X-ray flares, and type III radio bursts. This sequence of SEE events was extraordinary in terms of its frequency, especially on November 11 when SolO observed 13 SEE events at energies above ~10 keV, 11 events above ~65 keV, and three events above ~500 keV. This frequency of SEE events is much larger than the daily average at solar maximum (e.g., Wang et al. 2012), even though the period analyzed here occurred during the rising phase of solar cycle 25.

Despite the longitudinal separation between SolO and L1 (STA) of ~23° (8°) at the beginning of November 9 and of ~19° (4°) at the end of November 14, the most intense SEE events were observed at all these locations. Distinct patterns in the measured intensities (Figure 2) and anisotropies (Appendix B) at each spacecraft indicate the influence exerted by the varying magnetic connection of each spacecraft to the Sun, although modeling suggests that none of the spacecraft were directly connected to the sites of the solar phenomena associated with the SEE events (Figure 10).

The series of SEE events was associated with a sequence of EUV brightenings and jets from the periphery of the ARs 13140 and 13141. At the beginning of November 9, AR 13140 (13141) was centered around ~N28E14 (~N14E25), and by the end of November 14, it was at ~N28W62 (~N14W55). Although there are uncertainties in the spacecraft magnetic connectivity estimates (Figure 10), the two ARs were better connected with STA by November 13 and with L1 by November 14, resulting in the observation of SEE events with faster anisotropic rises to higher peak intensities at STA (L1) than at SolO by November 13 (November 14). By contrast, the closer magnetic connection of SolO with the ARs during November 10–12 led to the observation of events with rapid anisotropic increases and higher peak intensities at SolO, whereas the same events at STA and L1 displayed weaker anisotropies, gradual increases, and smaller intensities.

Remote-sensing observations during this sequence of SEE events show a plethora of solar phenomena that are commonly associated with such events. The abundance of EUV transient phenomena, including brightenings, jets, continuous ejections of material, and slow-rising structures that failed to erupt (Table 1), made the association between individual SEE events and these phenomena difficult to establish. We observe a general association between SEE events and X-ray flares, EUV emissions, and type III radio bursts (Figures 7 and 8). However, other factors, such as the magnetic connectivity between spacecraft and the sources of SEEs, also determine whether the SEEs can be reliably associated with these solar phenomena. During November 11 and 12, the association between these solar phenomena and the >10 keV SEE events observed by SolO was remarkable (Figures 7 and 8), presumably because the connection between SolO and the region where X-ray flares and EUV jets occurred was apparently better than on other days (Figures 10(a1)–(b1)). On the other hand (see Section 4), there are (i) small SEE events with no associated X-ray flare or EUV jet (these cases are usually associated with small EUV brightenings; see Table 1), and (ii) cases when intense solar phenomena occurred but an SEE event was not observed. In such cases, it is possible that energetic particles were produced, but no SEE event was observed due to poor magnetic connection; or that, during their propagation, the particles did not reach the open field lines connected to the observing spacecraft.

The observation of the most intense SEE events by SolO, STA, and near-Earth spacecraft has implications for the extent of the particle sources. These intense SEE events tend to be associated with extended EUV jets able to drive CFs that occur in close temporal association with HXR flares and with marked type III radio bursts extending from high frequencies to local Langmuir waves. Some of these most intense events were accompanied by $\lesssim$10 MeV proton intensity increases and heavy ions (i.e., the ion events #2, #3, #4, and #5 in Figure 5). We have analyzed whether these CFs were extended enough to establish magnetic connection with all these spacecraft. However, the results are not conclusive. First of all, we find that the observation of a CF does not imply the observation of an SEE event (e.g., Figure 11(d)). Additionally, the observed CFs propagated away from the estimated magnetic footpoints (Figure 11). It is possible that jets propagated toward higher altitudes in the corona being able to drive a compression wave or a shock capable of accelerating particles, but without leaving clear evidence of associated shock fronts on the solar disk. However, apart from propagating in the correct direction, conditions have to be appropriate for a jet to drive these structures and accelerate particles.

It has been suggested that the observation of relativistic SEEs in large widespread SEP events requires a contribution from electron acceleration at a CME-driven shock (e.g., Dresing et al. 2022). Figure 2(c) shows three clear 2.64–10.4 MeV electron intensity increases seen by SOHO/COSTEP/EPHIN (indicated by the three solid green circles in Figure 2(c)) that were associated with WL CMEs. However, these CMEs were modest in terms of their plane-of-sky speeds and widths: $V_{CME} = 175$ km s^{-1} and $\omega_{CME} = 45°$ for the relativistic SEE event at ~18:15 UT on November 12 (Figure 11(a)); $V_{CME} = 397$ km s^{-1} and $\omega_{CME} = 85°$ for the relativistic SEE event at ~13:05 UT on November 13; $V_{CME} = 321$ km s^{-1} and $\omega_{CME} = 74°$ for the relativistic SEE event at ~02:55 UT on November 14 (Figure 11(b)). Apart from these three WL-CME-associated relativistic SEE events, there were other smaller gradual relativistic electron intensity increases at L1. A relativistic electron increase at L1 on November 11 (first open green circle in Figure 2(c)) was most likely associated with the CF generated by the EUV jet at 11:26 UT (solar time) on November 11 from N12W10 that produced an SEE event at SolO at energies $\lesssim$2 MeV. As discussed in Section 4.2, the small 2.64–10.4 MeV electron intensity increase observed by SOHO/COSTEP/EPHIN early

on November 12 (second open green circle in Figure 2(c)) could be related to the CF originated at 04:25 UT (solar time). A possible additional very small 2.64–10.4 MeV electron intensity increase could be distinguished in the COSTEP/EPHIN green intensity curve in Figure 2(c) early on November 11, which was most likely associated with an EUV jet at 01:40 UT (solar time) on November 11 from N13W06, although a CF generated by the prior EUV jet at 01:25 UT (solar time) was still expanding and could have contributed to this SEE event. No CME could be associated with these three relativistic electron intensity enhancements on November 11 and early November 12, although their origins at longitudes near central meridian (as seen from Earth) make the observation of possible CMEs difficult.

Next, we consider whether, despite uncertainties in the estimated electron SRTs, they may provide insight into particle acceleration and transport in SEEs. We found some delays with respect to the onset of the EUV jets (Figure 9), which may result from the time needed (i) to accelerate particles; (ii) for the particles to propagate and reach open field lines connecting to the observing spacecraft; (iii) for the structures driven by the EUV jets, if able to accelerate particles, to reach open field lines allowing the accelerated particles to escape into interplanetary space; or (iv) for closed structures confining accelerated particles to become open and release the accelerated particles. Although not shown here, we find no correlation between the delays in Figure 9 and the angular distance between the field line footpoints and the site of EUV emissions, which tends not to favor (ii) or (iii) as the main cause. Most likely, multiple factors, such as different coronal magnetic field topologies and different particle source properties, may contribute to this lack of correlation between this angular distance and the particle SRTs. Precise modeling of the magnetic field configuration of these regions, as well as of the formation and propagation of jets, and of the particle acceleration and transport in these field topologies is required to elucidate the origin of the SRT delays.

Several of the SEE events are accompanied by ^{3}He-rich SEP events. Prior observations of ^{3}He-rich SEP events have shown associations with EUV jets that were triggered by minifilament eruptions (e.g., Bučík et al. 2018, 2023). In fact, it has been suggested that the origin of jets in both CHs (Sterling et al. 2015) and in the periphery of ARs (Sterling et al. 2024) always involves the eruption of a minifilament. In a statistical study of jets in CHs, Kumar et al. (2019b) found that about ∼70% of jets were associated with filament eruptions, but ∼30% showed no evidence of a minifilament although exhibited miniflare arcades and other eruptive signatures. In the series of events analyzed in this work, minifilaments were observed prior to the eruption of the jets in the periphery of the ARs in a few cases. Two cases are shown in Appendix C where raising minifilaments were clearly observed. In other cases, the pre-eruption filaments did not completely disappear, but a partial filament eruption or just the eruption of some filament strands might have occurred with the large-scale structure of the filament remaining mostly unaffected by the jet eruption (see similar examples in Mancuso et al. 2024). However, for most of the EUV jets in Table 1, the pre-eruption filaments were not detected. In particular, the repeated production of jets from the two nearby ARs, as well as the presence of suspended loop material from the two adjacent ARs, may have made it difficult to detect any pre-eruption filaments that might have been present (see similar cases in Sterling et al. 2024). Another possibility is that the generation of these jets did not require the eruption of a minifilament. However, establishing whether all the jets and associated SEE events discussed here were driven by a filament eruption interacting with the ambient magnetic field (e.g., Wyper et al. 2017; W. Wang et al. 2023) or just the narrow ejection of material produced by direct interchange magnetic reconnection requires the analysis of the magnetic topology of the source regions, which is beyond the scope of the present work.

The two peculiar SEE events on November 9 and November 14 observed at low electron energies ($\lesssim$45 keV and $\lesssim$58 keV, respectively) but rich in $\lesssim$1 MeV nucleon^{-1} heavy ions were not associated with clear jets or X-ray flares. The type III radio bursts associated with these two events started at frequencies below 1 MHz, indicating that the parent solar eruption was not able to drive an electron beam intense enough to generate radio emission from its inception. Both eruptions involved slow-rising confined EUV filaments (Figure 12), but how the SEE electrons and heavy ions might have escaped into interplanetary space cannot be determined. The solar origin of the episode of extremely high ^{3}He/^{4}He ratio early on November 10 (Figure 5) also cannot be resolved.

6. Summary

To summarize, the main results obtained in this study of a sequence of SEE events are the following:

1. A strong temporal and spatial association with HXR flares and EUV jets has been found for the most intense SEE events (Figures 7 and 8). Less intense and energetic SEE events may also be associated with EUV brightenings and small jets, but an HXR flare may be absent (Table 1).
2. Heavy-ion events associated with SEEs are generally related to extended jets and CFs (Table 2). Exceptions are ion events #1 and #6, which most likely originated with slowly rising confined EUV structures (Section 4.3).
3. The separation between the estimated magnetic field line footpoint and the location of the related EUV jet did not preclude the observation of the most intense SEE events at three locations spanning $\lesssim$22° in longitude. Nevertheless, this separation regulated the characteristics of the observed intensity-time profiles and anisotropies (Figure 2).
4. The anisotropic SEE events observed at ∼0.6 au displayed significant delays between the estimated SRTs and the onset of both EUV jets and HXR flares (Figure 9), confirming prior results obtained from statistical studies of SEE events observed at 1 au.
5. Some of the EUV jets were able to drive CFs that tended to be associated with intense SEE events. However, these CFs did not propagate toward the estimated field line footpoints of the observing spacecraft, and the detection of a CF did not necessarily imply the observation of an SEE event (Figure 11). Therefore, it is unclear from these events whether CFs are relevant for the acceleration of SEEs and their spread in the inner heliosphere.
6. A few CMEs were observed in association with the EUV jets, but they were modest in speed and size (Section 4.2), which suggests that they were unable to drive shocks that

could accelerate particles. In general, the observation of a wide and fast CME is not required for the acceleration and detection of a relativistic SEE event.

7. In the absence of broad particle sources, the spread of SEEs to distant heliospheric locations requires field configurations with field lines that extend in longitude and latitude that our methods to estimate magnetic connectivity did not reproduce. The presence of CHs near the origin of the EUV brightenings and jets (Figure 6) may also facilitate the escape of SEEs. Alternatively, SEE transport processes in either the solar corona and/or interplanetary space may allow SEEs accelerated from a narrow solar region to spread over a wide range of heliolongitudes, but these must maintain the large anisotropies observed at the onset of these SEE events.

Acknowledgments

We thank NASA and ESA for their support of the space missions whose data were used in this paper. Solar Orbiter is a mission of international cooperation between ESA and NASA, operated by ESA. SOHO is a mission of international cooperation between ESA and NASA, operated by NASA. STEREO is the third mission in NASA's Solar Terrestrial Probes program. SDO is a mission NASA's Living With a Star Program. ACE is a mission of NASA's Explorer Program. Wind is a mission of NASA's Heliophysics System Observatory. The Suprathermal Ion Spectrograph (SIS) is a European facility instrument funded by ESA under contract No. SOL.ASTR.CON.00004. Solar Orbiter postlaunch work for EPD/SIS is supported by NASA contract NNN06AA01C. Data used in this paper can be downloaded from soar.esac.esa.int/soar/, cdaweb.gsfc.nasa.gov, stereo-ssc.nascom.nasa.gov, and sdo.gsfc.nasa.gov. We acknowledge use of the SOHO/LASCO CME catalog generated and maintained at the CDAW Data Center by NASA and The Catholic University of America in cooperation with the Naval Research Laboratory. D.L. and I.G.R. acknowledge support from NAS. Living With a Star (LWS) program NNH19ZDA001N-LWS and the Guest Investigator Program NNH23ZDA001N-HGIO. I.G.R. also acknowledges support from the ACE mission. The UAH team acknowledges the financial support by the Spanish Ministerio de Ciencia, Innovacion y Universidades MCIU/AEI Project PID2019104863RBI00/AEI/10.13039/501100011033. A.W. acknowledges the support of the German Space Agency (DLR) under grant No. 50 OT 2304. A.K. acknowledges financial support from NASA NNN06AA01C (SO-SIS Phase-E) contract and HGIO grant 80NSSC24K0555. F. C. acknowledges financial support by an appointment to the NASA Postdoctoral Program at NASA Goddard Space Flight Center, administered by Oak Ridge Associated Universities through a contract with NASA. N.W. acknowledges support from the Research Foundation—Flanders (FWO-Vlaanderen, fellowship No. 1184319N). L.R. and A.N.Z. thank the Belgian Federal Science Policy Office (BELSPO) for the provision of financial support in the framework of the PRODEX Programme of the European Space Agency (ESA) under contract Nos. 4000134474 and 4000136424. A.A. acknowledges the Spanish Ministerio de Ciencia e Innovación project PID2022-136828NB-C41 that received financial support from MICIU/AEI/10.13039/501100011033 and FEDER, UE; the support through the "Center of Excellence María de Maeztu 2020-2023" award to the ICCUB (CEX2019-000918-M); and the support from the Departament de Recerca i Universitats de la Generalitat de Catalunya through grant 2021SGR00679.

Appendix A
Interplanetary Context

The left column of Figure A1 shows energetic particle intensities, magnetic field, and solar wind parameters collected by SolO from November 9 to November 17. Specifically, from top to bottom, we display (a1) energetic electron intensities averaged over all apertures of EPD/EPT (red and blue traces) and EPD/HET (green and orange traces); (b1) ion intensities averaged over all apertures of EPD/EPT (red, blue, and green traces) and proton intensities averaged over all apertures of EPD/HET (orange and black traces); (c1) magnetic field magnitude B; (d1) magnetic field elevation angle θ; (e1) magnetic field azimuthal angle ϕ in spacecraft centered radial–tangential–normal (RTN) coordinates measured by the SolO magnetometer instrument (SolO/MAG; Horbury et al. 2020); (f1) solar wind proton speed V_p; (g1) density N_p; and (h1) temperature T_p as measured by the Proton Alpha particle Sensor (PAS) of the Solar Wind Analyzer (SWA; Owen et al. 2020) on board SolO.

The middle column of Figure A1 shows from top to bottom (a2) energetic electron intensities averaged over all apertures of STA/SEPT (red, blue, and green traces) and electron intensities measured by STA/HET (orange and gray traces); (b2) ion intensities averaged over all the apertures of STA/SEPT (red and blue traces) and proton intensities measured by STA/LET (green and orange traces) and by STA/HET (black traces); (c2) B; (d2) θ; (e1) ϕ in RTN coordinates as measured by the magnetometer instrument on STA (Acuña et al. 2008); (f2) V_p; (g2) N_p; and (h2) T_p as measured by the Plasma and Suprathermal Ion Composition investigation (PLASTIC; Galvin et al. 2008) on board STA.

The right column of Figure A1 shows from top to bottom (a3) spin-averaged energetic electron intensities measured by the foil semiconductor detector telescopes (SO-F) of Wind/3DP (Lin et al. 1995; red, blue, and orange traces) and relativistic electron intensities measured by SOHO/COSTEP/EPHIN (gray trace); (b3) spin-averaged ion intensities measured by the open detector of the semiconductor telescopes (SO-SP) of Wind/3DP (top four traces showing only significant increases on November 14) and proton intensities measured by SOHO/COSTEP/EPHIN (magenta, orange, and black traces); (c3) B; (d3) θ; (e3) ϕ in RTN coordinates as measured by the magnetometer instrument on ACE (ACE/MAG; Smith et al. 1998); (f3) V_p; (g3) N_p; and (h3) T_p as measured by the Solar Wind Electron Proton Alpha Monitor (SWEPAM; McComas et al. 1998) on board ACE.

The most noticeable solar wind structure during the period shown in Figure A1 is the high-speed solar wind stream (indicated by HSS in Figure A1) observed by STA on November 11–12 and by ACE on November 12–13. This HSS was preceded by an enhanced magnetic field and solar wind density region between the HSS and the prior slow ($\sim$300 km s^{-1}) solar wind (as indicated by the label SIR in panels (c2) and (c3)). Plasma data from SolO/SWA were only available from 2022 November 11 onwards whereas SolO/MAG field data were available after mid-November 9. The short-duration magnetic field increase at SolO on mid-November 10 could be related to the SIR. However, assuming

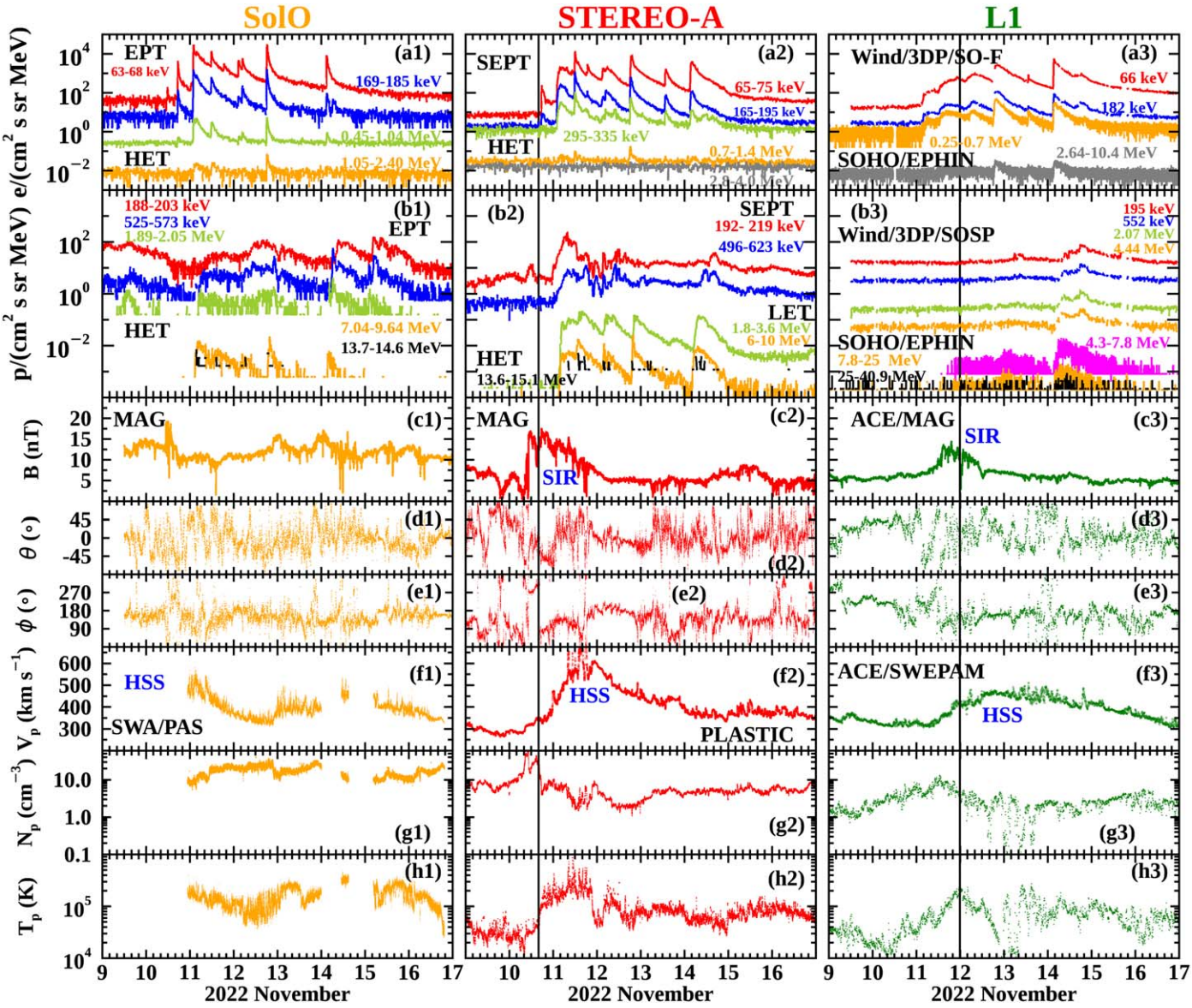

Figure A1. From top to bottom: Near-relativistic and relativistic electron intensities, energetic proton intensities, magnetic field magnitude B, magnetic field elevation angle θ, magnetic field azimuthal angle ϕ in spacecraft centered RTN coordinates, solar wind proton speed V_p, solar wind proton density N_p, and solar wind proton temperature T_p from 2022 November 9 to 17 measured by SolO (left column), STA (mid column), and at L1 (right column). See text for the specific instruments that collected these measurements. The solid vertical lines in the second and third columns indicate the passage of stream interface (SI) of the stream interaction region (SIR) preceding the passage of the solar wind high-speed stream (HSS) seen first by STA and later at L1. Existing SolO magnetic field and solar wind plasma data do not certify the passage of the SIR although the decreasing solar wind speed profile seen by SolO during November 11–12 suggests the passage of a preceding HSS.

that the HSS was a corotating structure, the SIR and HSS should have been observed at SolO late on November 8 and late on November 9, respectively. Unfortunately, this cannot be confirmed because of the SolO plasma data gap. Nevertheless, the decreasing solar wind speed seen by SolO during November 11–12 is consistent with the passage of a preceding HSS, with the short-duration magnetic field increase at SolO on mid-November 10 being interpreted as a local structure presumably unrelated to the SIR. Differences between the magnetic field and solar wind parameters' time profiles observed during corotation of solar wind streams by multiple spacecraft even at close proximity could be attributed to the different latitudes of where these spacecraft are located and/or temporal variations of the region where the HSS originated (e.g., Gómez-Herrero et al. 2011). The lower latitude of the near-Earth spacecraft during the period under study (see Figure 1) may be the reason why ACE observed a lower solar wind speed and a less compressed SIR than STA. The solid vertical lines in the middle and right columns of Figure A1 indicate the passage of the stream interface (SI) of the SIR identified as the time when the solar wind density within the SIR drops significantly (following the approach described in Richardson 2006).

According to the above interplanetary context, the sequence of SEE events observed by SolO on November 11 and 12 occurred during the passage of the tail of the HSS with the SIR already rotated beyond SolO location. The SEE events on November 13 and 14 occurred during the passage of a more irregular slow solar wind. Because of the uncertainty caused by the SolO/MAG and SolO/SWA data gaps, the low-energy

($\lesssim$45 keV) SEE event on 2022 November 9 associated with the ion event #1 (Figure 4) and the first SEE event on November 10 could have occurred during or after the passage of the SIR. The electron events at STA occurred once the SI of the SIR already passed over the spacecraft. Whereas the first two SEE events at this spacecraft in late November 10 and early November 11 occurred during the passage of the SIR, the subsequent electron events occurred during the HSS and decay phase of the HSS. By contrast, the first SEE events observed at L1 occurred prior to the passage of the SIR. The most intense SEE events at L1 occurred during the HSS passage already in late November 12 and on November 13 and 14. The electron events observed at L1 prior to and during the SIR passage showed a much more gradual increase and rounded smooth maximum intensity, whereas the subsequent electron events already in the HSS starting in late November 12 displayed a much faster rise to a peak intensity and a gradual decay.

Panels (a1) and (a2) of Figure A1 show that only the SEE events with SRTs, at ~01:42 UT, ~03:11 UT, and ~11:28 UT on November 11, and at ~17:52 UT on November 12, produced intensity enhancements extended to energies $\gtrsim$1 MeV. Figure 2(c) shows that only the event late on November 12 left a signal at energies above ~2.4 MeV in the EPD/HET detector. By contrast, panel (a3) of Figure A1 and Figure 2(c) show that at L1 the events at ~18:15 UT on November 12, ~13:05 UT on November 13, and early on November 14 left a clear signal in the SOHO/EPHIN electron detector at energies $\gtrsim$2.4 MeV. In Section 4.2, we analyze the solar activity associated with these more energetic events.

The panels (b1), (b2), and (b3) of Figure A1 show that the ion intensities at energies $\lesssim$2 MeV were more likely (i) influenced by the effects of the SIR (like the <600 keV ion increases early on November 11 at STA or the already elevated <600 keV ion intensities at the beginning of the plotted period on November 9 at SolO), and/or (ii) resulted from the merging of different injections (see also Figure 4). By contrast, the ion intensity enhancements at higher energies were a consequence of specific solar injections. Note that neither EPD/EPT, STA/SEPT, nor Wind/3DP/SO-SP intensities in panels (b1)–(b3) distinguish among different ion species. Therefore, the low-energy intensity traces plotted in panels (b1), (b2), and (b3) of Figure A1 may be constituted by a mix of the predominant proton population plus other heavy-ion species such as He particles. By contrast, EPD/HET, STA/LET, STA/HET, and SOHO/COSTEP/EPHIN provide proton intensities and allow us to distinguish those solar events that produced high-energy particles. In Section 4.2, we indicate the solar events that more likely produced also these high-energy proton intensity enhancements. However, the production of these high-energy protons was restricted to energies below ~13 MeV since only discrete counts were detected in the energy channels above this energy (black traces in panels (b1), and (b2) of Figure A1). The exception is the SEP event early on November 14 that produced >25 MeV proton intensity enhancements as observed by SOHO/COSTEP/EPHIN but not by the other spacecraft (see Section 4.2 for details on the solar origin of this event).

Appendix B
Energetic Electron Anisotropies

The four apertures of EPD/EPT and STA/SEPT allow us to analyze the energetic particle anisotropies at the three-axis stabilized SolO and STA spacecraft (e.g., Dresing et al. 2014; Gómez-Herrero et al. 2021), whereas the Wind spin-stabilized spacecraft allows the 3DP instrument to scan different regions of the sky and thus infer a more complete estimate of the 3D particle anisotropies. The pitch-angle coverage by the four apertures of EPD/EPT and STA/SEPT depends on the orientation of the magnetic field with respect to these telescopes. The four apertures of EPD/EPT cover four viewing directions that are to the north, to the south, along the nominal Parker spiral to the Sun, and along the nominal Parker spiral away from the Sun (see Figure 4 in Rodríguez-Pacheco et al. 2020). These apertures are designated north, south, sun, and asun, respectively. STA/SEPT apertures have a similar configuration. However, the configuration of STA during the period of these events was such that the sun aperture, which originally pointed toward the Sun along the direction of the nominal Parker spiral direction, pointed perpendicular to the nominal Parker spiral direction in the ecliptic in the $[-R, -T]$ quadrant, whereas the asun aperture happened to point in the opposite direction in the $[+R, +T]$ quadrant. The north and south apertures of STA/SEPT pointed perpendicular to the ecliptic plane in the south and north direction, respectively. Particle intensities measured by 3DP are stored into eight pitch-angle bins and usually provide a more complete coverage than EPD/EPT or STA/SEPT.

The top panel of Figure B1 shows the 46.7–86.6 keV electron intensities measured in each one of the four EPD/EPT apertures (sun in red, asun in yellow, north in purple, and south in teal). The second panel of Figure B1 shows the pitch-angle coverage scanned by the four EPD/EPT apertures. Since the magnetic field pointed mostly sunward ($\phi \sim 180°$), the sun aperture receives particles with large pitch angles, whereas the asun telescope scans small pitch angles. The third panel of Figure B1 shows the same pitch-angle coverage but color-coded according to the 46.7–86.6 keV electron intensities measured in each aperture. The fourth panel shows the magnetic field magnitude B (black trace) and the RTN components of the magnetic field vector. The bottom panel shows the first-order anisotropy coefficient defined as $A = 3\int_{-1}^{+1} I(\mu)\mu\, d\mu \Big/ \int_{-1}^{+1} I(\mu) d\mu$ where $I(\mu)$ is the pitch-angle dependent intensity measured in a given viewing direction, and μ is the average pitch-angle cosine for that direction. Details of how this anisotropy coefficient is computed can be found in Dresing et al. (2014), Brüdern et al. (2018), and references therein. The sign of A is given in terms of the magnetic field polarity. For a magnetic field polarity pointing sunward (like it was observed for this period; i.e., $\phi \sim 180°$ in Figure A1(e1)), $A < 0$ means particles flowing mostly away from the Sun. Large values of A (i.e., $|A| \gtrsim 2$) indicate highly anisotropic flows of particles, whereas small values (i.e., $|A| \lesssim 0.2$) indicate isotropic flows (e.g., Dresing et al. 2014). Figure B1 shows that the onset and peak of most of the 47–87 keV electron events at SolO were highly anisotropic whereas during the decay of the event the PADs evolved quickly to isotropic.

Figure B2 shows, with the same format as Figure B1, the anisotropy profiles of the 45–85 keV electron intensities measured by STA/SEPT. Owing to the peculiar configuration of STA during this period, the pitch-angle coverage is not appropriate to detect particles with large pitch-angle cosine (i.e., $|\mu| \sim 1$). Therefore, the particle intensities are mostly isotropic with the exception of (i) the first event observed late

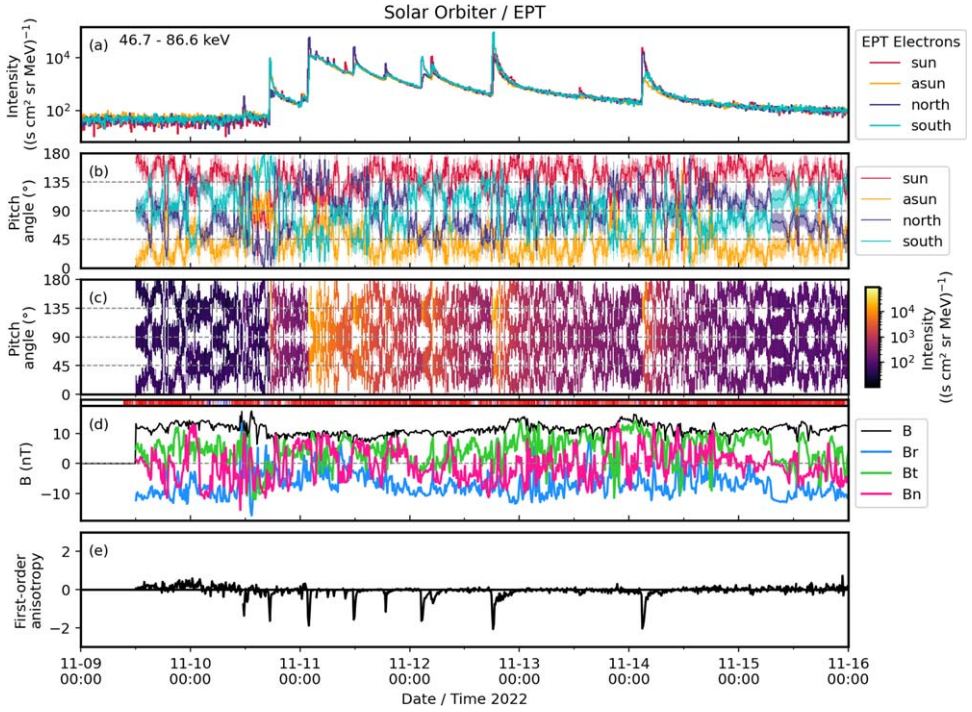

Figure B1. Time evolution of (a) 46.7–86.6 keV electron intensities measured in each one of the four EPD/EPT apertures; (b) pitch-angle coverage scanned by the four EPD/EPT apertures; (c) pitch-angle distribution color-coded according to the 46.7–86.6 keV electron intensities in the four apertures; (d) magnetic field magnitude B (black trace) and RTN components of the magnetic field vector B_r in blue, B_t in green, and B_t in magenta; (e) first-order anisotropy coefficient.

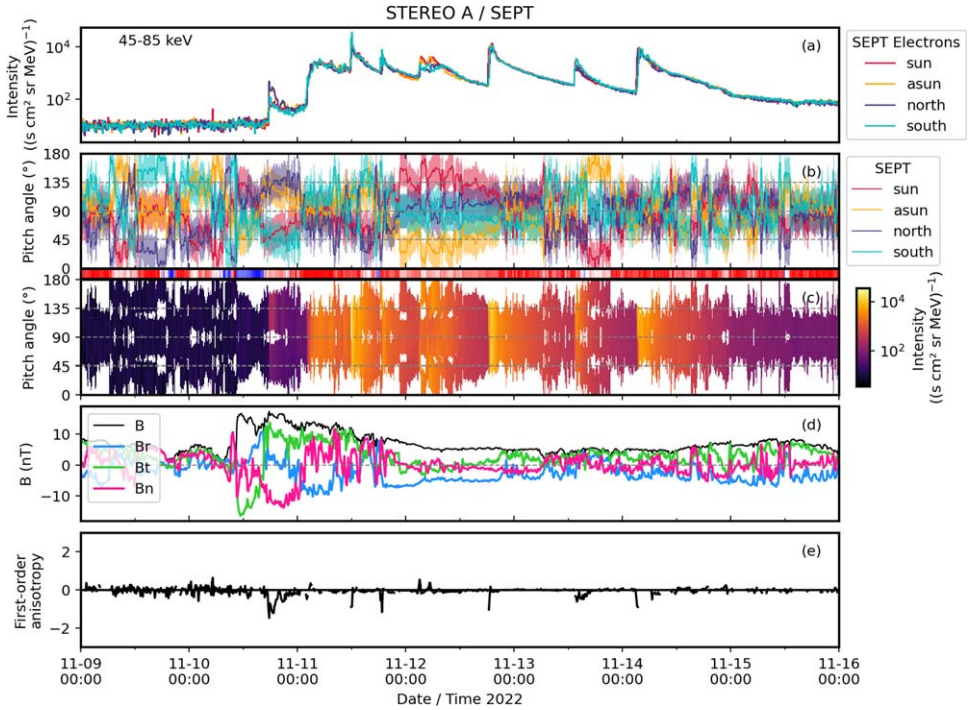

Figure B2. The same as Figure B1 but for the 45–85 keV electrons measured by STA/SEPT.

on November 10 that is dominated by the intensities in the north aperture because of the peculiar out-of-the-ecliptic field orientation observed after the SI of the SIR (see Figures A1(d2)), and (ii) the small SEE events early on November 12 when the magnetic field became radial ($\phi \sim 180°$ in Figure A1(e2)), and the sun telescope detected particles with pitch angles above 135° and hence the discrete positive values of A.

Figure B3 shows the 46.15–85.7 keV electron anisotropies as measured by Wind/3DP. The general appearance is that the gradual smooth electron intensity increases prior to November 13 displayed very weak anisotropies. The first electron

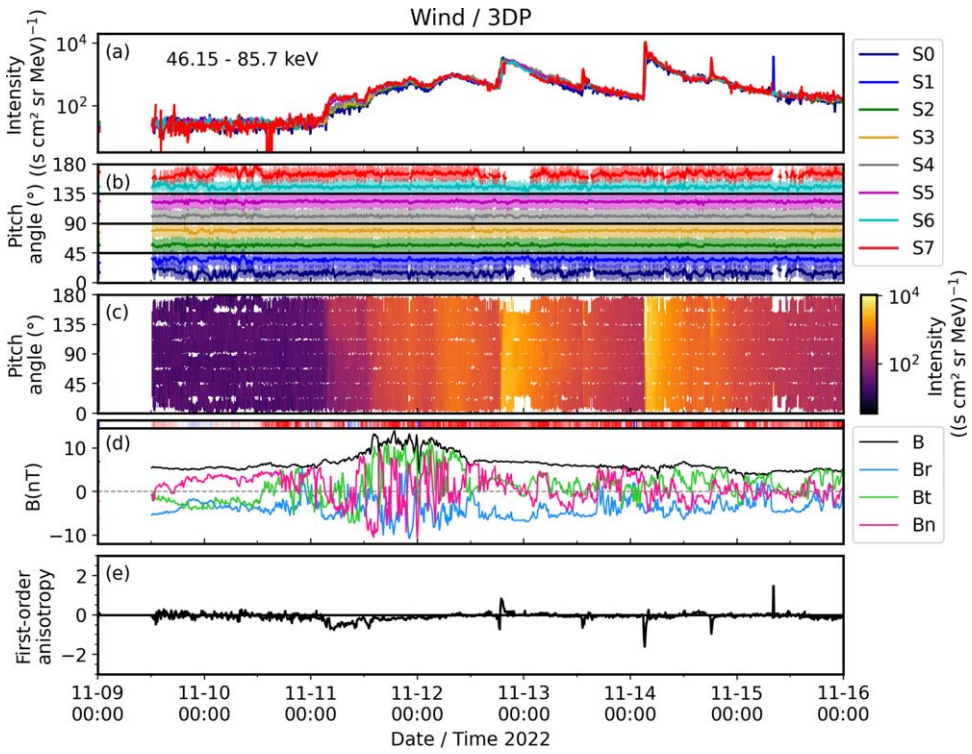

Figure B3. Time evolution of (a) 46.15–85.7 keV electron intensities measured by Wind/3DP binned in eight different pitch angles; (b) the eight pitch angles used to bin the measured intensities; (c) pitch-angle distribution color-coded according to the 46.15–85.7 keV electron intensities; (d) magnetic field magnitude B (black trace) and RTN components of the magnetic field vector B_r in blue, B_t in green, and B_t in magenta; (e) first-order anisotropy coefficient.

enhancement early on November 11, observed prior to the arrival of the SIR, showed some weak anisotropy ($|A| \lesssim 0.5$), whereas the rest of intensity increases were isotropic. During the onset of the electron event at the end of November 12, the lack of particle intensities for $|\mu| \sim 1$ does not allow us to completely evaluate A. For the events on November 14, when Wind established better magnetic connection with the particle sources (see Figure 10), the events showed rapid increases to peak intensities with larger anisotropies at the onset of the events.

Appendix C
Structure at the Origin of the Jets

Figure C1 shows two cases where minifilaments were clearly observed prior to the sequence of eruptions on (top row) November 12 between 17:32 UT and 18:01 UT and (bottom row) November 14 between 02:44 UT and 03:02 UT. From left to right, each panel shows (a) SDO/HMI line-of-sight magnetograms, (b) H_α (6563 Å) image obtained from the (top) El Teide and (bottom) Learmonth observatories,[31] and (c) SDO/AIA 304 Å images. The times at the bottom of each panel indicate when the images were taken. The arrows in the H_α and 304 Å indicate minifilament strands observed prior to the sequences of eruptions. The colored lines in the HMI panels indicate the position of the filaments that occurred to be in regions of mixed polarity and close to magnetic polarity inversion lines separating areas of two field polarities. In the top row of Figure C1, the yellow, green, and blue lines and arrows indicate the filament strands that erupted on November 12 at 17:32 UT, 17:45 UT, and 18:01 UT, respectively. Note that some material was seen to erupt at 17:52 UT from the same region, but no clear erupting filament could be discerned because of the brightening left by the prior eruption at 17:45 UT. The eruption at 18:01 UT drove the CF shown in Figure 11(a). In the bottom row of Figure C1, the yellow (green) lines and arrows indicate the filament eruption observed at 02:47 UT (03:02 UT) on November 14. The first of these eruptions was able to drive the CME displayed in Figure 11(b), but for which no CF in EUV images was observed.

For most of the EUV jets in the period under study (listed in Table 1), the pre-eruption filaments were not observed in either H_α or EUV images. This lack of observation might result from the fact that either the mechanism that generated the jets did not involve the eruption of a minifilament or the conditions for their observation were not appropriate. It has been pointed out that, in coronal jets produced by ARs, the erupting minifilaments may be hidden behind suspended absorbing material from the AR, making their detection difficult or impossible before they lose their minifilament character (Sterling et al. 2024). Similarly, the recurrent jets and brightenings occurring from the same region often overwhelm the observation where these possible subsequent jets might form. Another factor to consider is that, as previously observed (e.g., Sterling et al. 2024), magnetic eruptions making some AR jets often carry only thin minifilament strands that are hard to detect. Whether all the jets observed during this period were generated in the same fashion involving the eruption of a minifilament is beyond the scope of the present work. Therefore, the analysis of the specific mechanism that triggers each EUV eruption is not addressed here.

[31] nso.edu/data/nisp-data/h-alpha/

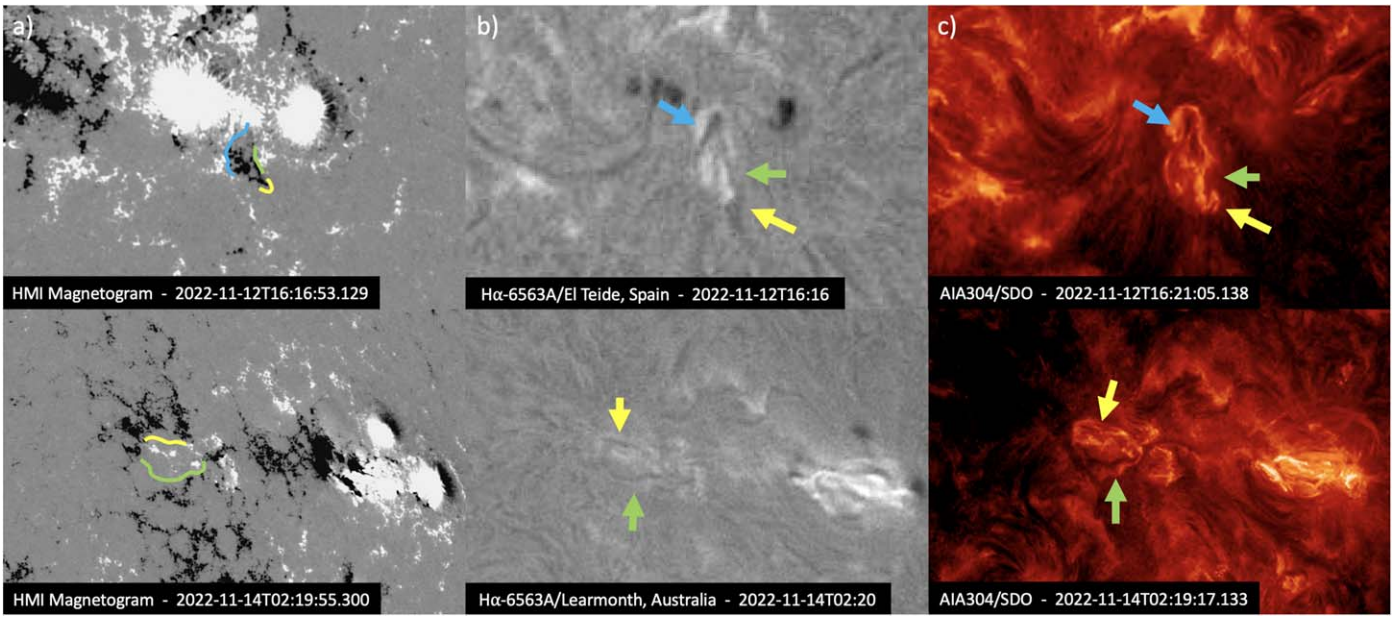

Figure C1. From left to right: SDO/HMI line-of-sight magnetograms, H_α images from GONG ground-based observatories, and SDO/AIA 304 Å images at the times indicated at the bottom of each panel observed prior to a sequence of (top row) three jets on November 12 and two jets (bottom row) on November 14. The yellow, green, and blue arrows and lines indicate the location of minifilaments observed prior to their eruption and were no longer observed after their eruption.

ORCID iDs

D. Lario https://orcid.org/0000-0002-3176-8704
L. A. Balmaceda https://orcid.org/0000-0003-1162-5498
R. Gómez-Herrero https://orcid.org/0000-0002-5705-9236
G. M. Mason https://orcid.org/0000-0003-2169-9618
V. Krupar https://orcid.org/0000-0001-6185-3945
C. Mac Cormack https://orcid.org/0000-0003-1173-503X
A. Kouloumvakos https://orcid.org/0000-0001-6589-4509
I. Cernuda https://orcid.org/0000-0001-8432-5379
H. Collier https://orcid.org/0000-0001-5592-8023
I. G. Richardson https://orcid.org/0000-0002-3855-3634
P. Kumar https://orcid.org/0000-0001-6289-7341
S. Krucker https://orcid.org/0000-0002-2002-9180
F. Carcaboso https://orcid.org/0000-0003-1758-6194
N. Wijsen https://orcid.org/0000-0001-6344-6956
R. D. Strauss https://orcid.org/0000-0002-0205-0808
N. Dresing https://orcid.org/0000-0003-3903-4649
A. Warmuth https://orcid.org/0000-0003-1439-3610
J. Rodríguez-Pacheco https://orcid.org/0000-0002-4240-1115
L. Rodríguez-García https://orcid.org/0000-0003-2361-5510
I. C. Jebaraj https://orcid.org/0000-0002-0606-7172
G. C. Ho https://orcid.org/0000-0003-1093-2066
R. Bučík https://orcid.org/0000-0001-7381-6949
D. Pacheco https://orcid.org/0000-0002-6176-4077
F. Espinosa Lara https://orcid.org/0000-0001-9039-8822
A. Hutchinson https://orcid.org/0000-0002-9362-7165
T. S. Horbury https://orcid.org/0000-0002-7572-4690
L. Rodríguez https://orcid.org/0000-0002-6097-374X
N. P. Janitzek https://orcid.org/0000-0001-6050-5033
A. N. Zhukov https://orcid.org/0000-0002-2542-9810
A. Aran https://orcid.org/0000-0003-1539-7832
N. V. Nitta https://orcid.org/0000-0001-6119-0221

References

Acuña, M. H., Curtis, D., Scheifele, J. L., et al. 2008, SSRv, 136, 203
Acuña, M. H., Ogilvie, K. W., Baker, D. N., et al. 1995, SSRv, 71, 5
Agueda, N., & Lario, D. 2016, ApJ, 829, 131
Arge, C. N., Henney, C. J., Koller, J., et al. 2010, in AIP Conf. Ser. 1216, Twelfth International Solar Wind Conf., ed. M. Maksimovic et al. (Melville, NY: AIP), 343
Bain, H. M., & Fletcher, L. 2009, A&A, 508, 1443
Battaglia, A. F., Wang, W., Saqri, J., et al. 2023, A&A, 670, A56
Bougeret, J. L., Goetz, K., Kaiser, M. L., et al. 2008, SSRv, 136, 487
Brown, J. C. 1971, SoPh, 18, 489
Brüdern, M., Dresing, N., Heber, B., et al. 2018, CEAB, 42, 2
Brueckner, G. E., Howard, R. A., Koomen, M. J., et al. 1995, SoPh, 162, 357
Bučík, R. 2020, SSRv, 216, 24
Bučík, R., Innes, D. E., Guo, L., Mason, G. M., & Wiedenbeck, M. E. 2015, ApJ, 812, 53
Bučík, R., Innes, D. E., Mall, U., et al. 2014, ApJ, 786, 71
Bučík, R., Innes, D. E., Mason, G. M., & Wiedenbeck, M. E. 2016, ApJ, 833, 63
Bučík, R., Innes, D. E., Mason, G. M., et al. 2018, ApJ, 852, 76
Bučík, R., Mason, G. M., Nitta, N. V., et al. 2023, A&A, 673, L5
Cane, H. V., McGuire, R. E., & von Rosenvinge, T. T. 1986, ApJ, 301, 448
da Silva, D. E., Wallace, S., Arge, C. N., & Jones, S. 2023, SpWea, 21, e2023SW003554
Dakeyo, J. B., Badman, S. T., Rouillard, A. P., et al. 2024, A&A, 686, A12
Domingo, V., Fleck, B., & Poland, A. I. 1995, SoPh, 162, 1
Dresing, N., Gómez-Herrero, R., Heber, B., et al. 2014, A&A, 567, A27
Dresing, N., Kouloumvakos, A., Vainio, R., & Rouillard, A. 2022, ApJL, 925, L21
Dulk, G. A., Steinberg, J. L., Lecacheux, A., Hoang, S., & MacDowall, R. J. 1985, A&A, 150, L28
Ergun, R. E., Larson, D., Lin, R. P., et al. 1998, ApJ, 503, 435
Fox, N. J., Velli, M. C., Bale, S. D., et al. 2016, SSRv, 204, 7
Galvin, A. B., Kistler, L. M., Popecki, M. A., et al. 2008, SSRv, 136, 437
Giacalone, J., & Jokipii, J. R. 2004, ApJ, 616, 573
Glesener, L., & Fleishman, G. D. 2018, ApJ, 867, 84
Glesener, L., Krucker, S., & Lin, R. P. 2012, ApJ, 754, 9
Gómez-Herrero, R., Malandraki, O., Dresing, N., et al. 2011, JASTP, 73, 551
Gómez-Herrero, R., Pacheco, D., Kollhoff, A., et al. 2021, A&A, 656, L3
Haggerty, D. K., & Roelof, E. C. 2002, ApJ, 579, 841
Harten, R., & Clark, K. 1995, SSRv, 71, 23
Heinemann, S. G., Temmer, M., Heinemann, N., et al. 2019, SoPh, 294, 144
Ho, G. C., Mason, G. M., & Allen, R. C. 2019, SoPh, 294, 33

Ho, G. C., Mason, G. M., Allen, R. C., et al. 2022, FrASS, 9, 939799
Ho, G. C., Roelof, E. C., Mason, G. M., Lario, D., & Mazur, J. E. 2003, AdSpR, 32, 2679
Horbury, T. S., O'Brien, H., Carrasco Blazquez, I., et al. 2020, A&A, 642, A9
Hou, Z., Tian, H., Su, W., et al. 2023, ApJ, 953, 171
Howard, R. A., Moses, J. D., Vourlidas, A., et al. 2008, SSRv, 136, 67
Kahler, S. W., Aurass, H., Mann, G., & Klassen, A. 2005, in IAU Symp. 226, Coronal and Stellar Mass Ejections, ed. K. Dere, J. Wang, & Y. Yan (Cambridge: Cambridge Univ. Press), 338
Kahler, S. W., Aurass, H., Mann, G., & Klassen, A. 2007, ApJ, 656, 567
Kahler, S. W., Reames, D. V., & Sheeley, N. R. J. 2001, ApJ, 562, 558
Kaiser, M. L., Kucera, T. A., Davila, J. M., et al. 2008, SSRv, 136, 5
Klein, K.-L. 2021, FrASS, 7, 105
Kouloumvakos, A., Mason, G. M., Ho, G. C., et al. 2023, ApJ, 956, 123
Kouloumvakos, A., Nindos, A., Valtonen, E., et al. 2015, A&A, 580, A80
Kouloumvakos, A., Rouillard, A. P., Wu, Y., et al. 2019, ApJ, 876, 80
Kozarev, K. A., Davey, A., Kendrick, A., Hammer, M., & Keith, C. 2017, JSWSC, 7, A32
Krucker, S., Battaglia, M., Cargill, P. J., et al. 2008, A&ARv, 16, 155
Krucker, S., Hurford, G. J., Grimm, O., et al. 2020, A&A, 642, A15
Krucker, S., Kontar, E. P., Christe, S., Glesener, L., & Lin, R. P. 2011, ApJ, 742, 82
Krucker, S., Larson, D. E., Lin, R. P., & Thompson, B. J. 1999, ApJ, 519, 864
Kruparova, O., Krupar, V., Szabo, A., Pulupa, M., & Bale, S. D. 2023, ApJ, 957, 13
Kumar, P., & Innes, D. E. 2015, ApJL, 803, L23
Kumar, P., Innes, D. E., & Cho, K.-S. 2016, ApJ, 828, 28
Kumar, P., Karpen, J. T., Antiochos, S. K., Wyper, P. F., & DeVore, C. R. 2019a, ApJL, 885, L15
Kumar, P., Karpen, J. T., Antiochos, S. K., et al. 2019b, ApJ, 873, 93
Kumar, P., & Manoharan, P. K. 2013, A&A, 553, A109
Lario, D., Kwon, R. Y., Richardson, I. G., et al. 2017a, ApJ, 838, 51
Lario, D., Kwon, R. Y., Riley, P., & Raouafi, N. E. 2017b, ApJ, 847, 103
Lario, D., & Roelof, E. C. 2010, in AIP Conf. Ser. 1216, Twelfth Int. Solar Wind Conf., ed. M. Maksimovic et al. (Melville, NY: AIP), 639
Lemen, J. R., Title, A. M., Akin, D. J., et al. 2012, SoPh, 275, 17
Li, B., Cairns, I. H., & Robinson, P. A. 2008, JGRA, 113, A06105
Li, B., Cairns, I. H., & Robinson, P. A. 2009, JGRA, 114, A02104
Lin, R. P. 1985, SoPh, 100, 537
Lin, R. P. 1990, in IAU Symp. 142, Basic Plasma Processes in the Sun, ed. E. R. Priest & V. Krishan (Dordrecht: Kluwer), 467
Lin, R. P., Anderson, K. A., Ashford, S., et al. 1995, SSRv, 71, 125
Lloyd, S. 1982, ITIT, 28, 129
Luhmann, J. G., Curtis, D. W., Schroeder, P., et al. 2008, SSRv, 136, 117
MacNeice, P., Elliott, B., & Acebal, A. 2011, SpWea, 9, S10003
Maksimovic, M., Bale, S. D., Chust, T., et al. 2020, A&A, 642, A12
Maksimovic, M., Souček, J., Chust, T., et al. 2021, A&A, 656, A41
Mancuso, M., Jing, J., Wang, H., et al. 2024, Triennial Earth-Sun Summit, Abstract 302–03, https://agu.confex.com/agu/TESS24/meetingapp.cgi/Paper/1493835
Mason, G. M. 2007, SSRv, 130, 231
Mason, G. M., Gold, R. E., Krimigis, S. M., et al. 1998, SSRv, 86, 409
Mason, G. M., Korth, A., Walpole, P. H., et al. 2008, SSRv, 136, 257
Mason, G. M., Nitta, N. V., Bučík, R., et al. 2023a, A&A, 669, L16
Mason, G. M., Roth, I., Nitta, N. V., et al. 2023b, ApJ, 957, 112
Massa, P., Hurford, G. J., Volpara, A., et al. 2023, SoPh, 298, 114
McComas, D. J., Bame, S. J., Barker, P., et al. 1998, SSRv, 86, 563
Mewaldt, R. A., Cohen, C. M. S., Cook, W. R., et al. 2008, SSRv, 136, 285
Mondal, B., Vadawale, S. V., Del Zanna, G., et al. 2023, ApJ, 955, 146
Moore, R. L., Cirtain, J. W., Sterling, A. C., & Falconer, D. A. 2010, ApJ, 720, 757
Müller-Mellin, R., Böttcher, S., Falenski, J., et al. 2008, SSRv, 136, 363
Müller-Mellin, R., Kunow, H., Fleißner, V., et al. 1995, SoPh, 162, 483
Müller, D., St. Cyr, O. C., Zouganelis, I., et al. 2020, A&A, 642, A1
Murphy, N., Smith, E. J., & Schwadron, N. A. 2002, GeoRL, 29, 2066
Musset, S., Jeunon, M., & Glesener, L. 2020, ApJ, 889, 183
Nitta, N. V., Bučík, R., Mason, G. M., et al. 2023, FrASS, 10, 50
Nitta, N. V., Mason, G. M., Wang, L., Cohen, C. M. S., & Wiedenbeck, M. E. 2015, ApJ, 806, 235
Nitta, N. V., Mason, G. M., Wiedenbeck, M. E., et al. 2008, ApJL, 675, L125
Nitta, N. V., Reames, D. V., De Rosa, M. L., et al. 2006, ApJ, 650, 438
Nolte, J. T., & Roelof, E. C. 1973, SoPh, 33, 241
Odermatt, J., Barczynski, K., Harra, L. K., Schwanitz, C., & Krucker, S. 2022, A&A, 665, A29
Owen, C. J., Bruno, R., Livi, S., et al. 2020, A&A, 642, A16
Pesnell, W. D., Thompson, B. J., & Chamberlin, P. C. 2012, SoPh, 275, 3
Ragot, B. R., & Kahler, S. W. 2008, ICRC (Mérida), 1, 147
Raouafi, N. E., Patsourakos, S., Pariat, E., et al. 2016, SSRv, 201, 1
Reames, D. V. 1990, ApJS, 73, 235
Reames, D. V. 2021, FrASS, 8, 164
Reames, D. V., Dennis, B. R., Stone, R. G., & Lin, R. P. 1988, ApJ, 327, 998
Reames, D. V., Meyer, J. P., & von Rosenvinge, T. T. 1994, ApJS, 90, 649
Reames, D. V., von Rosenvinge, T. T., & Lin, R. P. 1985, ApJ, 292, 716
Reid, H. A. S., & Kontar, E. P. 2018, ApJ, 867, 158
Reid, H. A. S., & Vilmer, N. 2017, A&A, 597, A77
Richardson, I. G. 2006, Recurrent Magnetic Storms: Corotating Solar Wind, doi:10.1029/167GM06 ed. R. McPherron et al., Vol. 167 (Washington, DC: American Geophysical Union), 45
Rodríguez-García, L., Gómez-Herrero, R., Dresing, N., et al. 2023, A&A, 670, A51
Rodríguez-Pacheco, J., Wimmer-Schweingruber, R. F., Mason, G. M., et al. 2020, A&A, 642, A7
Roth, I., & Temerin, M. 1997, ApJ, 477, 940
Rouillard, A. P., Pinto, R. F., Vourlidas, A., et al. 2020, A&A, 642, A2
Scherrer, P. H., Schou, J., Bush, R. I., et al. 2012, SoPh, 275, 207
Schrijver, C. J., & De Rosa, M. L. 2003, SoPh, 212, 165
Shen, Y. 2021, RSPSA, 477, 217
Shibata, K., Ishido, Y., Acton, L. W., et al. 1992, PASJ, 44, L173
Simnett, G. M., Roelof, E. C., & Haggerty, D. K. 2002, ApJ, 579, 854
Smith, C. W., L'Heureux, J., Ness, N. F., et al. 1998, SSRv, 86, 613
Sterling, A. C., Moore, R. L., Falconer, D. A., & Adams, M. 2015, Natur, 523, 437
Sterling, A. C., Moore, R. L., & Panesar, N. K. 2024, ApJ, 960, 109
Stone, E. C., Frandsen, A. M., Mewaldt, R. A., et al. 1998, SSRv, 86, 1
Ugarte-Urra, I., Upton, L., Warren, H. P., & Hathaway, D. H. 2015, ApJ, 815, 90
Ugarte-Urra, I., & Warren, H. P. 2012, ApJ, 761, 21
Vainio, R., Valtonen, E., Heber, B., et al. 2013, JSWSC, 3, A12
Volpara, A., Massa, P., Perracchione, E., et al. 2022, A&A, 668, A145
von Rosenvinge, T. T., McDonald, F. B., Trainor, J. H., Van Hollebeke, M. A. I., & Fisk, L. A. 1978, ITGE, 16, 208
von Rosenvinge, T. T., Reames, D. V., Baker, R., et al. 2008, SSRv, 136, 391
Voshchepynets, A., Krasnoselskikh, V., Artemyev, A., & Volokitin, A. 2015, ApJ, 807, 38
Wang, L., Krucker, S., Mason, G. M., Lin, R. P., & Li, G. 2016, A&A, 585, A119
Wang, L., Lin, R. P., Krucker, S., & Gosling, J. T. 2006, GeoRL, 33, L03106
Wang, L., Lin, R. P., Krucker, S., & Mason, G. M. 2012, ApJ, 759, 69
Wang, M., Chen, B., Yu, S., et al. 2023, ApJ, 954, 32
Wang, W., Battaglia, A. F., Krucker, S., & Wang, L. 2023, ApJ, 950, 118
Wang, Y. M., Pick, M., & Mason, G. M. 2006, ApJ, 639, 495
Wibberenz, G., & Cane, H. V. 2006, ApJ, 650, 1199
Wiedenbeck, M. E., Mason, G. M., Cohen, C. M. S., et al. 2013, ApJ, 762, 54
Wilson, L. B. I., Brosius, A. L., Gopalswamy, N., et al. 2021, RvGeo, 59, e2020RG000714
Wimmer-Schweingruber, R. F., Janitzek, N. P., Pacheco, D., et al. 2021, A&A, 656, A22
Wyper, P. F., Antiochos, S. K., & DeVore, C. R. 2017, Natur, 544, 452
Wyper, P. F., & DeVore, C. R. 2016, ApJ, 820, 77
Wyper, P. F., DeVore, C. R., & Antiochos, S. K. 2018, ApJ, 852, 98
Wyper, P. F., DeVore, C. R., & Antiochos, S. K. 2019, MNRAS, 490, 3679
Yashiro, S., Gopalswamy, N., Michalek, G., et al. 2004, JGRA, 109, A07105